Bulletin of the Seismological Society of America, Vol. 107, No. 4, pp. 1828–1848, August 2017, doi: 10.1785/0120160334

Nonlinear Attenuation of *S* Waves by Frictional Failure at Shallow Depths

by Norman H. Sleep and Nori Nakata

Abstract Strong *S* waves produce dynamic stresses, which bring the shallow subsurface into nonlinear anelastic failure. The construct of coulomb friction yields testable predictions about this process for strong-motion records. Physically, the anelastic strain rate increases rapidly with increasing dynamic stress, and dynamic stress is proportional to the difference between total strain and anelastic strain. Nonlinear models of vertically propagating *S* waves in layered media confirmed and illustrated analytical inferences. The effective coefficient of friction bounds (clips amplitude) the resolved horizontal acceleration normalized to the acceleration of gravity. There is a tendency for the random signal from vertically propagating *S* waves to become transiently circularly polarized at the maximum (clipped) resolved acceleration, as the acceleration component perpendicular to the current acceleration adds weakly the resolved acceleration. Frictional attenuation does not preferentially suppress high-frequency signal; it cannot be modeled by increasing ordinary linear attenuation. In addition, an effect of shallow cohesion is to allow brief pulses of strong high-frequency acceleration to reach the surface. Frictional attenuation within deep overpressured aquifers suppresses shaking recorded at the surface, but does not simply clip amplitude at a given resolved acceleration. The anelastic strain rate increases slowly with stress within shallow muddy sediments. The accelerations from reverberations within such layers can exceed $1g$.

Introduction

Horizontal motions from strong *S* waves are a major concern for structural engineers. Strong shaking from large events often continues over many cycles, allowing surface shaking at the *S*-wave resonant frequency of the ground to build up. Qualitatively with major earthquakes, the extensive fault planes act as numerous high-frequency sources with significant durations (e.g., Joshi *et al.*, 2014; Sandeep *et al.*, 2014; Otarola and Ruiz, 2016).

The purpose of this article is to examine the approximate rheology for nonlinear behavior when impinging *S* waves generate high dynamic stresses and strains within the shallow subsurface. Intuitively, shallow stiff rocks come into frictional failure and dissipate energy. The nonlinear interaction of *S* waves with other types of seismic waves provides evidence on the reality of frictional behavior in the uppermost tens of meters (Sleep and Nakata, 2015, 2016). A net effect is that nonlinear attenuation reduces the overall wave amplitude at the surface to less than it would have been in a fully elastic medium. We give most of our attention to potentially observable effects in the time domain that can be constrained by scaling relationships. Observation of these effects would support that shallow rocks in fact fail in friction. Mathematically, the frequency domain provides eigenfunctions for linear elastic waves, but not for nonlinear waves. We continue to mention frequency with this caveat, because the term is widely used and the concept is very useful for qualitative discussions of nonlinear waves.

Approximate analytical and numerical modeling of shallow reverberations and nonlinearity of *S* waves is tractable because they refract into nearly vertical paths in the low-velocity shallow subsurface. Compact analytical expressions and fast numerical methods arise for exactly vertical ray paths and laterally homogeneous structure.

We obtain simple scaling relationships for complicated situations that provide limits for peak ground acceleration (PGA) for *S* waves. We begin by comparing the implications of frictional rheology and flow-law rheology in general with the widely used Masing rules. Then, we discuss simplifications that accrue with the approximation of vertically propagating *S* waves. For tractable quantification, we apply a nonlinear numerical model for vertically ascending *S* waves modified from the works of Sleep and Erickson (2014) and Sleep and Nakata (2015) to laterally stratified rocks with wave motion in both horizontal directions. We consider the effects of a deep overpressured aquifer and reverberation of strong *S* waves in shallow soil as societal applications.

As a caveat, 3D structure often has significant effects on surface shaking. For example, Thompson *et al.* (2012) found that laterally homogeneous layers often do not give acceptable models of low-amplitude wave transfer functions between collocated borehole and surface stations in Japan. Acceptable laterally homogeneous results are more frequent for California sites within flat-lying sediments (Afshari and Stewart, 2015). At the sites where laterally homogeneous calculations fail to represent shaking, impinging S waves may produce significant vertical motion and P waves may produce significant horizontal motion. Fully 3D, nonlinear codes are available (Roten *et al.*, 2014) and applicable if shallow seismic structure is well constrained. Our purposes are to illustrate rheological behavior that could be incorporated in such models and to provide scaling relations that will help in formulating models and understanding their results.

Rheology

Numerical codes exist for nonlinear propagation of seismic waves in 3D (e.g., Roten *et al.*, 2014). Such codes represent frictional failure, but have not been used to model high-frequency vertical S waves within the shallow subsurface. Our intent is to model rocks in which friction provides plausible rheology to find testable implications and help in planning more onerous 3D numerical models. We present general features of flow-law rheology, which includes the well-known case of coulomb frictional failure. Then, we briefly discuss the widely used Masing rules for soil failure to put our frictional models for vertical S waves into context.

Frictional Rheology

We introduce rheology beginning with the implications of the Drucker and Prager (1952) failure criterion for a rock mass in 3D. In general, this failure criterion depends on the second invariant of the deviatoric stress tensor $|\tau|$ and the mean stress $P \equiv \sigma_{ii}/3$, in which σ is the full stress tensor compression positive.

Vertical S waves do not change mean stress. They produce shear tractions in the horizontal x and y directions on horizontal planes perpendicular to depth z, that is, τ_{xz} and τ_{yz}. The failure criterion then reduces to

$$|\tau|^2 = \tau_{xz}^2 + \tau_{yz}^2 + \tau_{\text{other}}^2 \le (\rho g \mu z + C)^2, \tag{1}$$

in which τ_{other} represents other (properly normalized) components of the deviatoric stress tensor that are not zero at the free surface including the effects of the near-field velocity pulse, Love waves, and Rayleigh waves. The parameter C is cohesion, the strength at zero vertical normal stress, ρ is density, and μ is the coefficient of friction.

The plastic failure criterion in equation (1) (in which the anelastic strain rate goes from immeasurably slow to exceedingly fast at failure) is a special case of a flow-law rheology. In general, components of the anelastic strain rate tensor $\varepsilon'_{ij,\text{an}}$ are proportional to the components of deviatoric stress tensor τ_{ij} and thus have the sense to relax this stress. For vertical S waves, the vertical displacement and its spatial derivatives are zero. The vertical gradients of the horizontal anelastic displacement U yield the nonzero components of the anelastic strain rate tensor: $2\varepsilon'_{xz,\text{an}} \equiv \partial^2 U_{x,\text{an}}/\partial z \partial t$ and $2\varepsilon'_{yz,\text{an}} \equiv \partial^2 U_{y,\text{an}}/\partial z \partial t$. These components are proportional to the horizontal shear tractions: $(\varepsilon'_{xz,\text{an}}, \varepsilon'_{yz,\text{an}}) \propto (\tau_{xz}, \tau_{yz})$. Roten *et al.* (2014) modeled plastic failure as flow-law failure over a small finite stress range for numerical tractability.

In a flow-law formulation, the deviatoric stress depends linearly on the elastic strain, that is, on the difference between the total deviatoric strain e_{ij} and anelastic strain $\varepsilon_{ij,\text{an}}$. For vertical S waves, the horizontal shear traction for simple shear on horizontal planes is $\tau_{iz} = 2G(e_{iz} - \varepsilon_{iz,\text{an}})$, in which i is a horizontal direction, and G is the shear modulus. The rate of energy dissipation per volume is the product of resolved anelastic horizontal strain rate and resolved horizontal shear traction (which here have the same orientation) $|\tau||\varepsilon'|$. Nonlinear attenuation of a seismic wave is thus strongly linked to anelastic strain. These simple features are readily generalized to 3D as in the calculations of Roten *et al.* (2014), but with significant computational burden. Alternative formulations in which nonlinear energy dissipation does not lead to macroscopic anelastic strains include Masing rules discussed in the next section.

In a simple flow-law approximation, the shear modulus G retains its initial value, yielding testable predictions. Our code can represent a slight or even a moderate decrease in the shear modulus from damage $\partial G/\partial t \propto -|\varepsilon'|$ and its subsequent healing $\partial G/\partial t > 0$. We consider effect within shallow muddy sediments in the Application to Reverberating Signal within Soft Sediments section as an application in which the strain rate increases gradually with shear traction. Our numerical code in the Appendix cannot represent liquefaction and transient strengthening of saturated sediments associated with sudden dilatancy (e.g., Bonilla *et al.*, 2011).

Frictional failure of rock masses is likely to behave as (flow-law) stress-dependent creep rather than sharp plastic failure in equation (1). The construct of rate and state friction strives to represent the anelastic part of this process, traditionally for sliding on a fault plane (e.g., Dieterich, 1979; Ruina, 1983). Following Sleep and Nakata (2015), the 1D anelastic strain rate (at the start of failure at given constant normal traction P) is

$$\varepsilon' = \varepsilon'_{\text{ref}} \exp\left[\frac{\tau - \mu_{\text{ref}} P}{aP}\right] \psi_{\text{old}}^{-b/a}, \tag{2}$$

in which $\varepsilon'_{\text{ref}}$ is the reference strain rate, μ_{ref} is the reference coefficient of friction, τ is the dynamic shear traction, and a and b are dimensionless physical parameters of the order of 10^{-2}. The parameter ψ_{old} is the state variable at the start of shaking. The slip rate increases as the exponential of τ/aP. A small relative change in τ changes the strain rate from immeasurably slow to very fast. The state variable decreases once slip begins, further increasing the strain rate at a given stress. The net effect is that an individual fracture in the rock either fails or stays intact. Near-total stress drop may occur on some fractures. A rock with a large number of identical horizontal fractures might fail plastically, maintaining the failure stress, or it might fail to a low stress with a large stress drop.

A more realistic rock model should represent numerous fractures with different state variables, orientations, and different coefficients of friction. Some of these fractures likely have prestresses leftover from residual stresses failure in previous seismic events. These fractures fail preferentially when they are favorably oriented with respect to the new dynamic stress. Still, the macroscopic (potentially predictable) strain rate (averaged over many fractures) is expected to go from very slow to quite fast over a range of dynamic tractions, but more gradually than predicted by equation (2). The anelastic strain rate is then formally

$$\varepsilon'_{iz,\mathrm{an}} = \left[\frac{\tau_{iz}}{|\tau|}\right] F(|\tau|/P), \tag{3}$$

in which F is a steep monotonic function with dimensions of strain rate. The bracket indicates that anelastic deformation occurs with the sense to relieve the deviatoric stress.

Masing Rules

For comparison, engineers and seismologists often use Masing rules to model nonlinear failure of the shallow subsurface during strong shaking (e.g., Hartzell *et al.*, 2004; Assimaki *et al.*, 2008, 2011; Phillips and Hashash, 2009; Tobita *et al.*, 2010; Santisi d'Avila *et al.*, 2012; Kaklamanos *et al.*, 2015; Zalachoris and Rathje, 2015; Groholski *et al.*, 2016). This construct has different implications than flow-law rheology, as it relates dynamic stress τ to dynamic strain ε. Numerical modeling of failure using Masing rules is beyond the scope of this article, as the code in the Appendix is unsuitable for that task.

We continue qualitatively with the implications for vertically ascending S waves. Horizontal tractions on horizontal planes produce strain, that is, vertical gradients in the horizontal displacement U. If the system is started at rest from an unstressed $\tau = 0$ and unstrained $\varepsilon = 0$ state, the initial low-amplitude strain in one horizontal dimension is proportional to the stress

$$\tau = G_{\mathrm{int}}\varepsilon, \tag{4}$$

in which G_{int} is the elastic shear modulus (Fig. 1a). The differential shear modulus $G_{\mathrm{diff}} \equiv \partial\tau/\partial\varepsilon$ decreases at large strains. The differential shear modulus returns to the elastic shear modulus on strain reversal at point A. In Figure 1, this sense of strain continues to point B. Strain reversal occurs again and the strain returns to point A. Attenuation during a cycle from A to B to A is proportional to the area bounded by the hysteresis curve. The formalism can be extended to account for more complicated stress–strain histories. Generalization to 3D is feasible (Santisi d'Avila *et al.*, 2012). In addition, the stress for significant nonlinear behavior may be based on coulomb friction and hence increase with depth (Hartzell *et al.*, 2004). (This modification retains the feature of frictional attenuation discussed in the remaining sections, that dynamic acceleration normalized to the acceleration of gravity is bounded by the effective coefficient of friction.) Some formulations are based on the rheology of unconsolidated sand (e.g., Tobita *et al.*, 2010).

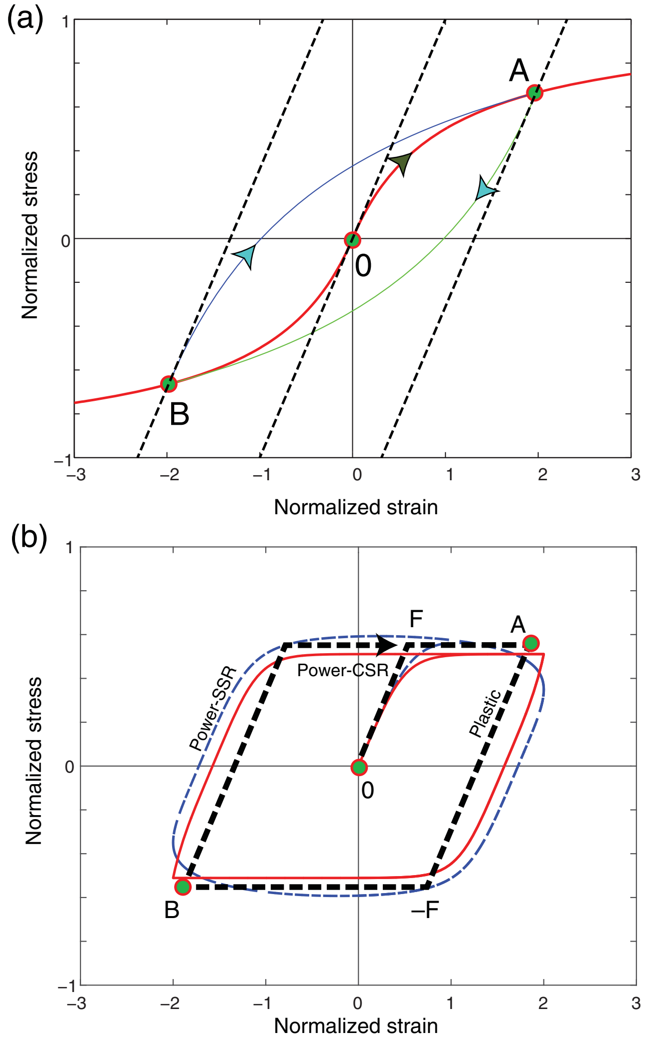

Figure 1. (a) Schematic diagram of Masing rules. The material starts at zero stress and strain (point 0). For small strains, the material behaves elastically and the stress–strain point moves parallel to the dashed line that extrapolates in normalized strain–strain units (in which $G_{\mathrm{int}} \equiv 1$) to (1,1). The slope of the curve decreases with increasing strain. At point A, the sense of strain change reverses. The initial deformation is parallel to the dashed elastic line. The strain and stress go to point B by following the lower thin curve. On strain reversal, the strain–stress path returns to point A (upper thin curve). (b) The path (thick dashed line) for a plastic material is similar. The material reaches its yield stress at point F and continues at this stress to point A. The sense of strain reverses and the material deforms elastically to point −F in which the stress remains constant until the sense of strain reverses at point B. The loops for power-law deformation are similar to the plastic curve and differ slightly between sinusoidal strain rate (SSR, thin dashed line) and constant strain rate (CSR, solid line). The color version of this figure is available only in the electronic edition.

Masing rules, however, have unattractive features for a physics based, as opposed to a semiempirical, model of nonlinear attenuation that motivate consideration of flow-law alternatives. First, various formulations with numerous parameterizations are available to fit theoretical curves (as in Fig. 1a) to experimental data (e.g., Assimaki *et al.*, 2011; Groholski *et al.*, 2016). It is not obvious how these formulations relate to the microphysics of fractured rock and thus how to extrapolate from the laboratory to the field. More importantly, strain rate is not involved. The theoretical curve in Figure 1a is the same if the material is driven at 100 or 0.01 Hz. In rheological terms, no further strain occurs when soil is maintained at constant stress and the stress remains constant if the soil is maintained at constant strain. Yet, one might expect real soil to flow viscously under a large constant load and stress to relax under constant strain. With regard to rocks, the anelastic strain rate depends on stress in the formalism of rate and state friction in equation (2) (e.g., Dieterich, 1979; Ruina, 1983). In both frictional cases unlike Masing rules, a slight drop in the magnitude of deviatoric stress does not change the sense of the anelastic strain rate. These features would become evident in laboratory experiments. We are not aware of any suitable studies on relevant earth materials.

Conversely, Masing rules do provide similar predictions to flow-law rheologies in simple experiments in which the material is driven back and forth between macroscopic displacements of $\pm D$, that is, strains of $\pm\varepsilon$ as in Figure 1a. For two examples, we consider that a material is driven around a simple hysteresis loop for plastic and flow-law rheologies.

The stress–strain loop for a plastic material is a special case of Masing rules (Fig. 1b). The strain remains constant if the stress is maintained slightly below the failure stress. It is also a special case of a flow law, in which the strain rate goes from extremely slow to extremely fast at the failure stress so that there is no explicit rate dependence in the loop in Figure 1b. Thus, rapid strain would continue indefinitely, if the material were driven at a stress infinitesimally greater than the yield stress. The material behaves elastically until the failure stress is reached at point F and this stress is maintained with further strain until point A. This is equivalent to $G_{\text{int}} = 0$ at the failure stress. The sense of strain then reverses and the failure stress in the opposite direction is reached at point −F. Further strain continues until point B where the sense strain reverses again. The material then follows a parallelogram-shaped hysteresis loop.

A flow-law material follows a similar hysteresis loop when driven with these simple strain conditions. In the example, the strain rate is proportional to the stress to the third power (Fig. 1b). The imposed strain rate is constant with either strain sense or varies sinusoidally. In both cases, the initial deformation is essentially elastic. In the former case, stress increases until the anelastic strain rate balances the imposed strain rate. In the latter, the imposed strain rate is low near the peak stress allowing anelastic strain to modestly reduce the stress. The Masing curves in Figure 1a could be made to more closely resemble the flow-law curves in Figure 1b by adjusting the parameters of either simulation.

Thus, the differences between flow laws and Masing rules become evident in the laboratory only when the material is driven in a complicated manner (see Kausel and Assimiki, 2002). Conversely, the Masing rules may provide an adequate description of nonlinear behavior in shallow subsurface for simple earthquake waves, especially if one seeks only the overall diminution of energy. This article concerns the complicated signal and its details in the time domain, in which friction-based flow-law rheologies provide testable predictions.

Frictional Failure of Shear Waves in the Shallow Subsurface

We continue with the well-known theory of frictional failure for vertical *S* waves. Our presentation is intended to apply to originally stiff exhumed sedimentary and crystalline rocks and likely to gravel. The mathematics apply to soft mud with the caveat that the anelastic strain rate may increase slowly with stress. Our intent is to have simple general implications that can be tested against earthquake records.

Following Sleep and Erickson (2014), the laterally homogeneous momentum equation in the horizontal directions indicates that acceleration is everywhere proportional to the vertical gradient of the horizontal shear traction

$$\rho A_i = \frac{\partial \tau_{iz}}{\partial z}, \tag{5}$$

in which i is the tensor index for a horizontal direction, ρ is the density, A is the acceleration, τ is the stress tensor, and z is the depth. We use equation (5) to present a general derivation for failure stresses to illustrate the expected behavior of flat-lying sedimentary rocks. The failure stress is proportional to the effective stress

$$\tau_{\text{fail}} = \mu(P_{\text{lith}} - P_{\text{fluid}}) \approx \mu \int_0^z (\rho - \rho_{\text{fluid}}) g \, dZ, \tag{6}$$

in which μ is the coefficient of friction, P_{lith} is lithostatic pressure, P_{fluid} is the fluid pressure, and g is the acceleration of gravity. The first equality is general and includes the case of artesian fluid pressure. The approximate equality assumes that fluid pressure depends on the density of the overlying fluid ρ_{fluid}, which is a function of Z, the dummy variable for depth.

The vertical derivative of the approximate failure stress in equation (6) is

$$\frac{\partial \tau_{\text{fail}}}{\partial z} = \mu(\rho - \rho_{\text{fluid}}) g + \frac{\partial \mu}{\partial z} \int_0^z (\rho - \rho_{\text{fluid}}) g \, dZ. \tag{7}$$

The $\partial\mu/\partial z$ term represents that some beds may have higher coefficients of friction than other beds. For example, clay-rich sedimentary units are expected to have lower coefficients of friction than clay-poor ones (e.g., Ikari *et al.*, 2009; Kohli and Zoback, 2013). However, horizontal shear tractions are continuous between the beds. For quarter-wavelengths longer than the thicknesses of a few beds, the weak beds with low coefficients of friction μ_{weak} fail first and the failure stress is not reached within the strong beds with high coefficients of friction. The effective coefficient of friction of a depth range of beds is approximately that of the weakest beds. In 3D, the coefficient of friction of a rock mass is approximately that of the weakest throughgoing cracks.

The vertical gradient of shear traction in equation (5) is thus approximately limited by the vertical gradient of failure stress for weak beds in equation (7):

$$\rho|A| \le \mu_{\text{weak}}(\rho - \rho_{\text{fluid}})g, \tag{8a}$$

in which absolute value sign indicates the resolved maximum component of horizontal acceleration. (The gradient term in equation (7) is assumed to be ~0, because a series of beds fails at the frictional strength of its weakest member. Our numerical code in the Appendix can represent depth-dependent coefficients of friction.) Solving equation (8a) yields the well-known result that (at failure) the normalized maximum acceleration (acceleration in g's) is the effective coefficient of the rock mass

$$\frac{|A|}{g} \le \mu_{\text{weak}}\left[\frac{\rho - \rho_{\text{fluid}}}{\rho}\right]. \tag{8b}$$

The densities and the coefficient of friction in equations (8a) and (8b) pertain to conditions at a given depth within the rock mass where weak beds exist, rather than depth averages from the surface.

We continue with vertical S waves that reflect off the free surface. We assume isotropy, constant density, constant shear modulus, no fluid pressure, and constant coefficient of friction μ to compact notation. For the ith component of a monochromatic wave, the displacement is

$$U_i = U_{0i}[\cos(\omega t + kz) + \cos(\omega t - kz)], \tag{9}$$

in which the first term is the upcoming wave, the second term is the downgoing wave, U_{0i} is the upcoming maximum amplitude at great depth, ω is the angular frequency, t is the time, and k is the wavenumber. The shear traction is

$$\tau_{iz} = -G\frac{\partial U_i}{\partial z} = GkU_{0i}[\sin(\omega t + kz) - \sin(\omega t - kz)], \tag{10}$$

in which G is the shear modulus. The shear traction reaches its overall maximum of $2\tau_{0i} \equiv 2GkU_{0i} = 2\rho V_{0i}\beta$, in which quarter-wavelength depth $\pi/(2k)$, $\sin(kz) = 1$, and $\beta = \sqrt{G/\rho} = \omega/k$ is the S-wave velocity. (The quarter-wavelength depth maximum is obtained from $\sin(\omega t \pm kz) = \sin(\omega t)\cos(kz) \pm \cos(\omega t)\sin(kz)$, which leaves the $\cos(\omega t)\sin(kz)$ term from the difference in equation 10.) In the final equality, V_{0i} is the peak particle velocity of the ascending wave from differentiation of equation (9) by time and applying $\beta = \omega/k$.

At shallow depths in which $kz < 1$, the first term of the Taylor series expansion of equation (10) ($\sin(kz) \approx kz$) yields the well-known result that the peak shear stress is

$$|\tau| = 2U_0k^2Gz = 2\rho V_0\beta kz = 2\rho A_0 z \le \rho g\mu z, \tag{11}$$

recovering the result in equation (8b) at the failure stress. Thus, a circle bounds observed values of (A_x, A_y):

$$\left(\frac{A_x}{g}\right)^2 + \left(\frac{A_y}{g}\right)^2 \le \left[\mu + \frac{C}{\rho g z}\right]^2 - \left[\frac{\tau_{\text{other}}}{\rho g z}\right]^2, \tag{12}$$

in which the left side is the square of the resolved acceleration in equation (8b). The right side generalizes the frictional strength on the right side of equation (8b) to the more general expression in equation (1) with cohesion and other sources of deviatoric stress. The cohesion term increases the diameter of the circle and the appropriate depth in equation (12) is crudely the quarter-wavelength depth of the dominant frequency on an acceleration seismogram. The τ_{other} term reduces the diameter of the predicted circle at times in which surface waves and the near-field velocity pulse are significant.

This relationship (12) is approximately applicable for the Lucerne record of the 1992 Landers earthquake (Fig. 2a). Strong accelerations continued for ~6 s at Lucerne (Fig. 2b). Sleep and Nakata (2015) noted that the near-field velocity pulse likely produced additional dynamic stresses in equation (12) and hence complicated nonlinearity beneath Lucerne. The deviatoric stress increased as the rupture tip approached Lucerne and then decreased as fault slip occurred adjacent to Lucerne. In addition, strong P waves may have transiently affected the normal traction on vertical planes (Sleep and Nakata, 2015) and the structure is not fully laterally homogeneous (Sleep, 2012).

Figure 2 still serves to show simple ways to examine real data. We use it to qualitatively discuss expected features with regard to numerical models. From equation (12), cohesion is likely to be important very near the free surface where the lithostatic stress is small. In addition, real seismographs are moored at a finite depth, which has the net effect of cohesion. Both of these features suppress failure from and nonlinear attenuation of high-frequency waves with very shallow quarter-wavelength depths.

Numerical Calculations

We modify the numerical model of Sleep and Erickson (2014) and Sleep and Nakata (2015) to compute the anelastic strain rate in equation (3) in two horizontal dimensions in the Appendix. The code requires constant density, which is here 2250 kg/m^3, appropriate for gravel and perhaps hard-rock regolith. This value is too low for more or less intact crystalline rocks. The time step Δt is 0.00025 s, which oversamples the uppermost layer at 0.1-m grid spacing in the

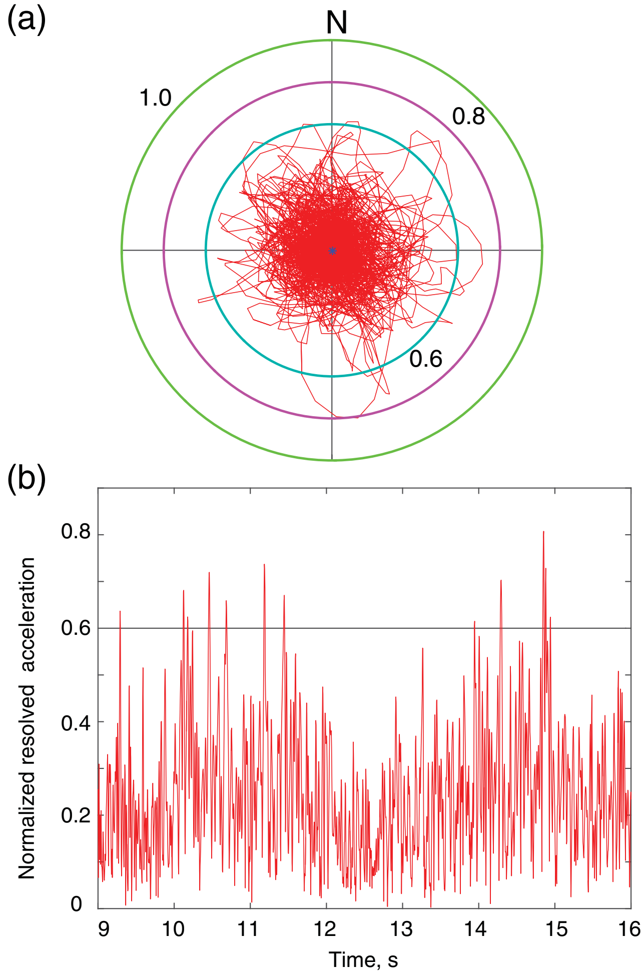

Figure 2. (a) Polar plot of horizontal acceleration from the 1992 Landers earthquake recorded at Lucerne station. Circles show resolved acceleration normalized to the acceleration of gravity. Several excursions are between 0.6 and 0.8. (b) The resolved horizontal acceleration versus time. In a simple model, the resolved normalized acceleration would clip at the effective coefficient of friction. Data and origin of time are from Iwan and Chen (1995) and Chen (1995). The color version of this figure is available only in the electronic edition.

Appendix. Failure cracks in a real rock could well be spaced further apart than 0.1 m.

The numerical method is free of dispersion when the product $\Delta t\beta$ of the time step and the shear-wave velocity is the depth range in each numerical element in the Appendix. Here, the shear modulus within each numerical element remains constant during the calculations. Thus, we ignore the modest effects of any new cracks produced when the rock fails in friction in the majority of our calculations. Our method by allowing the shear modulus within elements to vary during shaking can represent the large dynamic decreases in stiffness that sometimes occur in soils (e.g., Assimaki *et al.*, 2011; Nakata and Snieder, 2011; Wu and Peng, 2011). The appropriate failure criterion and recovery rheology for such soil materials are discussed in the Application to Reverberating Signal within Soft Sediments section. Liquefaction is beyond the scope of this article.

The rate and state formulation in equation (2) implies that cracks that have just failed should be weaker for later failure during subsequent strong shaking. Rubinstein and Beroza (2004) resolved this effect by observing decreases in the low-amplitude seismic velocity after the M_{w} 6.9 Loma Prieta mainshock and later M_{L} 5.4 Chittenden earthquake. Rocks that had already been shaken in the earlier event were damaged by weaker shaking in the later event. In our case, we would predict that PGA in equation (8b) would decrease during prolonged shaking as the state variable in equation (2) decreased. We do not see this effect for the Lucerne record in Figure 2b in which the strongest resolved acceleration occurred late in the shaking. Thus, we did not include weakening in our numerical model, even though we could have done so.

We make additional approximations to keep the numerical approach simple. We ignore changes in normal tractions and hence the behavior of friction during changes in normal traction (Linker and Dieterich, 1992; Perfettini *et al.*, 2001; Wang *et al.*, 2014), appropriately for vertical S waves. We make no attempt to include changes in the rake direction of horizontal shear traction and horizontal strain rate in the rheology, that is, damage tensors (Sleep, 1998). The finite mass, overburden weight, and elastic properties of buildings are not included (e.g., Petrovic and Parolai, 2016). Qualitatively, the mass per area of the building becomes important in the subsurface when compared with the mass per area of rock above the quarter-wavelength depth. Where feasible, engineers often remove compliant soil to place foundations of large edifices on stiffer bedrock or insert pilings into bedrock. The effects in this paragraph could be included in more sophisticated numerical codes in 3D, productively to model strong waves that impinge on a dense borehole array or a large structure.

We present two idealized models of the shallow Earth that are loosely based on the structure at the Lucerne station near the Landers earthquake rupture (Sleep, 2012; Fig. 3). In the layer model, the S-wave velocity is 400 m/s above 9.95 m depth and 3000 m/s below that. In the gradient model, the S-wave velocity is 400 m/s above 0.55 m depth and increases to 3000 m/s at 99.15 m depth. The layer model is intended to produce strong resonances and the gradient model weak ones.

Impinging Signal

With regard to the impinging signal, ordinary attenuation at depth is expected to suppress high frequencies if the earthquake source is far from the station. However, strong earthquake waves sometimes trigger small earthquakes in the shallow subsurface (Fischer, Peng, *et al.*, 2008; Fischer, Sammis, *et al.*, 2008; Fischer and Sammis, 2009). High-frequency signal from these events does reach surface stations that are immediately above the events. The dynamic acceleration may even exceed 1g (Aoi *et al.*, 2008; Sleep and Ma, 2008; Tobita *et al.*, 2010). Our numerical code does not attempt to model such events, which occur over a finite lateral area and hence require 3D calculations. We include some high-frequency signal to represent this effect in the boundary

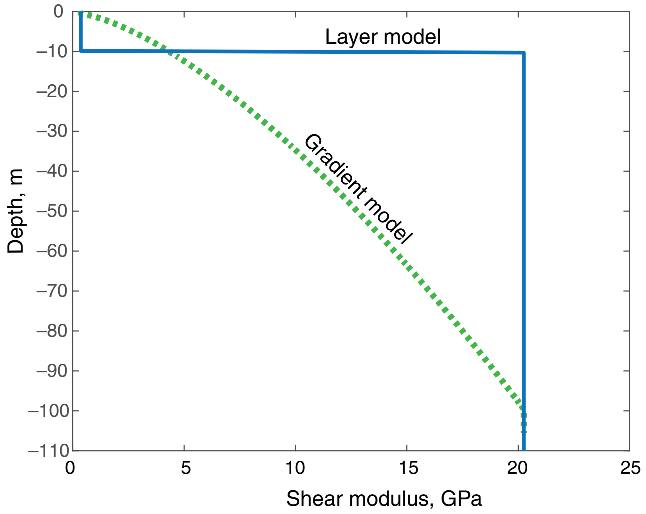

Figure 3. The shear moduli for the layer model (solid) and the gradient model (dashed) as a function of depth. The color version of this figure is available only in the electronic edition.

condition at the base of the model in the Appendix. This numerical signal ascends without ordinary attenuation toward the surface where it encounters nonlinear effects. We provide examples with sinusoidal and broadband ascending waves.

Synthetic Sinusoidal Signal

We begin with an unrealistic model of the ascending waves to illustrate basic features of nonlinear attenuation that might be observed with more realistic broadband signal. We define our orthogonal components as north–south and east–west for convenience. Our ascending wave consists of 10-Hz circularly polarized waves with north–south and east–west components 90° out of phase. High-frequency (160 Hz) waves ascend only on the east–west component (Fig. 4d). The 10 Hz waves are in resonance with the layer in Figure 3 and the 160 Hz waves are out of resonance. The upcoming east–west signal begins 0.025 s before the north–south signal and ends 0.025 before the north–south signal. We give attention to the circularly polarized signal when both components are present.

The computed acceleration of the nonlinear waves is less than that in the elastic model, as expected (Fig. 4a). In detail, behavior differs from that of ordinary attenuation, which preferentially suppresses high-frequency waves (Fig. 4c). From equation (12), high-frequency stresses persist briefly and do not have time to cause large anelastic strains. In terms of stresses, the linear low-frequency ω_L component ascending with peak dynamic velocity V_L and peak dynamic acceleration A_L generates a peak stress of $2\rho\beta A_L/\omega_L = 2\rho\beta V_L$ at the quarter-wavelength depth. An out-of-phase high-frequency ω_H component generates stress of $\rho\beta A_H/\omega_H = \rho\beta V_H$ below its quarter-wavelength depth, in which V_H and A_H are the ascending dynamic velocity and acceleration. In the case that the high-frequency and low-frequency components generate similar accelerations and hence comparable dynamic stresses very near the free surface, the low-frequency component dominates the dynamic stress at its quarter-wavelength depth because $V_L > V_H$ in which $A_L \approx A_H$ and by assumption $\omega_L \ll \omega_H$. In addition, elastic and kinetic energy of the wave scale with particle velocity squared. The high-frequency wave transports little wave energy to damage subsurface rock and aboveground structures.

High frequencies on the east–west component are diminished near the times of overall high east–west acceleration, as expected. High frequencies are also present on the north–south component, although they are not present in the upcoming north–south signal. Mathematically, both the east–west and north–south signals contribute to the resolved horizontal acceleration in equation (10). The north–south component is suppressed when the high-frequency east–west component adds to the resolved acceleration.

In 2D, as viewed on a polar plot (Fig. 4b), the acceleration is to the first order circularly polarized near the maximum resolved acceleration as intended. High-frequency accelerations perpendicular to the low-frequency acceleration (tangential to the circle) do not add greatly to the resolved acceleration in equation (10) and hence are not strongly suppressed.

In general, clipping at a given acceleration has a different overall effect on wave amplitude than on linear attenuation. For a simple example, we compare the sinusoid $A_0 \sin(\omega t)$, in which A_0 is $1g$ acceleration clipped to $\pm 0.7g$, with the unclipped sinusoid $A_1 \sin(\omega t)$, in which A_1 is $0.7g$. Both have the same PGA $0.7g$. However, the integral of the clipped sinusoid and hence peak ground velocity (PGV) is greater for the clipped sinusoid than the unclipped sinusoid. The root mean square amplitude and the peak displacement are also larger for the clipped sinusoid. This exercise shows that the constructs of PGA, PGV, and linear damping factor provide incomplete understanding of frictional attenuation.

Synthetic Broadband Signal

Current dynamic earthquake rupture calculations of large earthquakes do not resolve high-frequency signal. Lavallée and Archuleta (2005) related the statistics of PGA to the statistics of high stress-drop asperities on the fault plane. Semiempirical methods predict statistically ascending high-frequency signal at hard-rock sites (e.g., Stewart *et al.*, 2015). Empirical methods to predict shaking duration are available (Afshari and Stewart, 2016). For large events including the 2011 Tohoku mainshock, one may sum waves from numerous strong-motion generation areas on the fault plane (e.g., Joshi *et al.*, 2014; Sandeep *et al.*, 2014; Otarola and Ruiz, 2016). We bypass these approaches and assume that the impinging waves are strong enough to produce shallow nonlinear behavior.

Thus, we do not explicitly consider the earthquake source, because we are interested in the physics-based limits that shallow nonlinear frictional attenuation places on PGA.

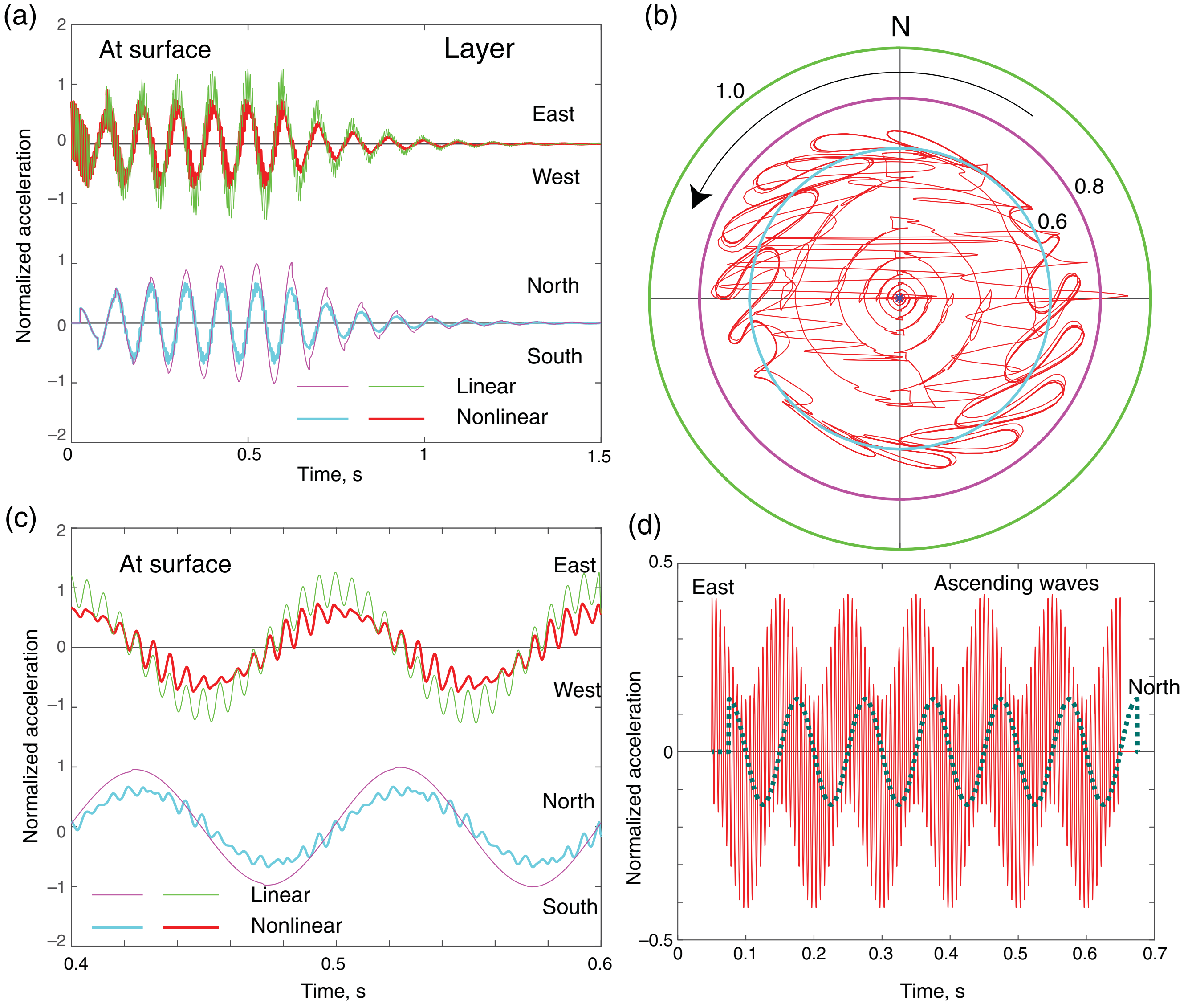

Figure 4. Layer model with upcoming sinusoidal signal. (a) The computed east–west (E–W) and north–south (N–S) signals at the surface. The resonant 10-Hz linear signal builds over the initial oscillations. The nonlinear signal is approximately clipped. Origin of time is arbitrary. (b) Polar plot of the nonlinear signal, as in Figure 2. The signal is approximately circularly polarized once both components are active. The computed resolved acceleration would clip sharply at the effective coefficient of friction for a plastic rheology. The modeled-resolved acceleration is not sharply clipped because the anelastic strain rate in equations (3) and (A4) increases gradually with resolved shear traction. High-frequency signal perpendicular to the low-frequency acceleration is not strongly suppressed. (c) The signal windowed between 0.4 and 0.6 s. High frequency is present on the N–S nonlinear signal, but not in the linear signal, which does not couple with the east component. (d) The upcoming signal with original time arbitrary. The waves would produce this normalized surface acceleration within an elastic half-space. E–W signal is denoted by thin line; N–S signal is denoted by thick dashed line. The color version of this figure is available only in the electronic edition.

Intuitively, it is unlikely that there is anything special in the earthquake source region with regard to the local site threshold in wave amplitude for shallow nonlinear behavior, so waves exceeding this threshold should sometimes ascend toward the surface. Our main criterion in generating synthetic ascending signal is that it has high enough amplitude that the predicted effects of nonlinearity become evident in the calculations. Other criteria are that the signal has duration similar to the recording at Lucerne in Figure 2b and that it is random with the two components uncorrelated. We used the Gaussian white noise “wgn” function in MATLAB to generate uncorrelated east–west and north–south broadband upcoming time series (Fig. 5a). The plotted upcoming wave has been filtered to have a realistic frequency range (Fig. 5b) that might represent strong waves from a nearby event in analogy to the Lucerne record (Fig. 2). The ends of the signal were tapered to avoid sharp initial and final accelerations. The mean accelerations are zero so that the dynamic velocity returns to zero at the end of shaking. The signals are approximately symmetric near the middle so that the dynamic

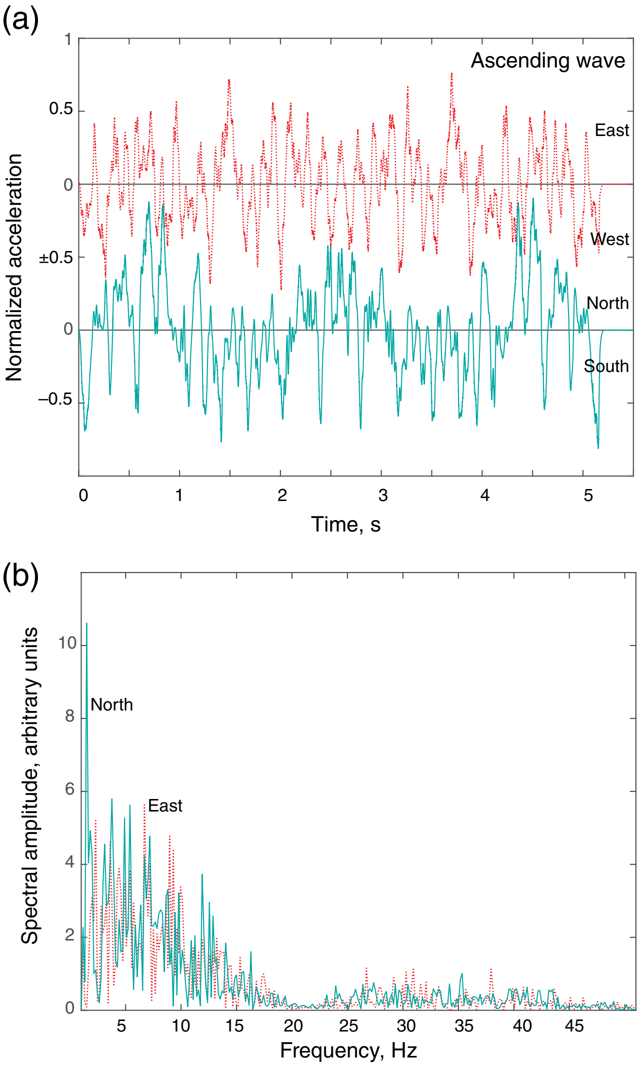

Figure 5. The random signal used in the remaining models. E–W signal is denoted by dotted line; N–S signal is denoted by solid line. (a) The normalized acceleration in the time domain normalized to that which would be produced within an elastic half-space. The duration of strong shaking is intended to be similar to that observed at Lucerne in Figure 2b. Time origin is start of signal. (b) The spectral amplitude includes a side lobe above 25 Hz. The color version of this figure is available only in the electronic edition.

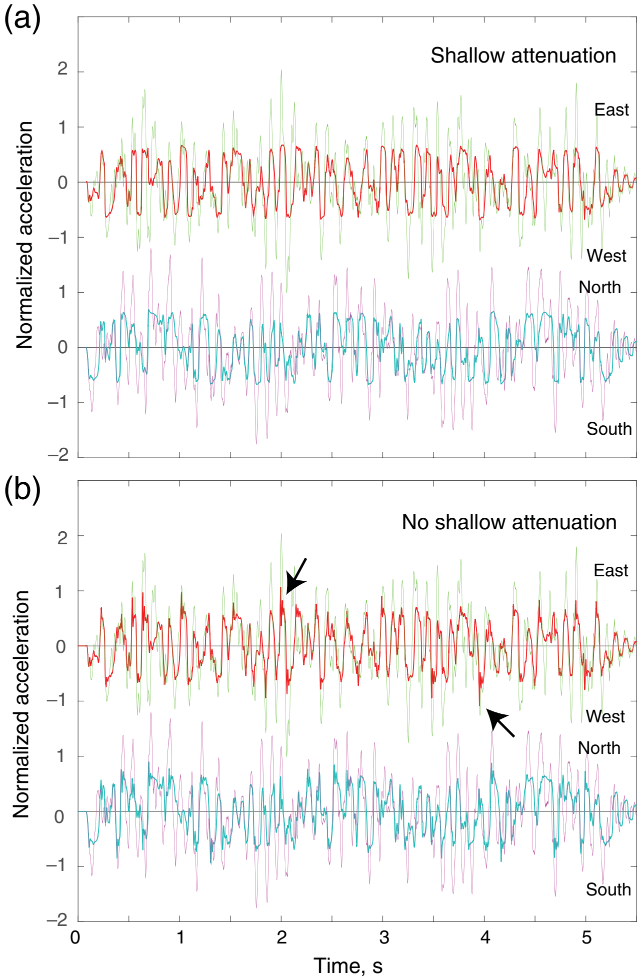

Figure 6. The normalized acceleration for the layer model. Linear models are denoted by thin lines; nonlinear models are denoted by thick lines. Time origin is arbitrary. (a) The models include shallow nonlinear attenuation, the 10 Hz resonance is evident. The nonlinear signal appears clipped. (b) Models with no shallow attenuation. High-frequency spikes (arrows) arrive at the surface. The color version of this figure is available only in the electronic edition.

displacements return to zero. This processing scheme yielded stronger low-frequency signal on the north–south component than on the east–west component because of the vagaries of the initial white noise time series for the two components.

A high-frequency side lobe exists between 25 and 45 Hz (Fig. 5b). We retained this feature to illustrate the fate of any earthquake-generated high-frequency signal, as well as high frequencies generated by very shallow triggered earthquakes just beneath the station. Our method for generating the signal also caused the acceleration at every fifth time step to differ slightly from its neighbors. Such an 800 Hz signal ($=1/5\Delta t$) would not likely be present in real events, and conventional seismographs would not detect it. We retained this feature as it shows that the numerical method is not dispersive. The small kinks also serve as 0.00125 s time marks.

Figure 6a shows the response for the layered model. There is the expected tendency for ~10 Hz signals to be amplified. The signal on both components appears clipped. Clipping at a resolved acceleration is more evident on the polar plot (Fig. 7a). As with the sinusoidal model, the signal is transiently circularly polarized near the maximum resolved acceleration (here, in either direction), as higher frequency accelerations perpendicular (tangential) to the main acceleration are not strongly suppressed. The waves continued to reverberate linearly for some time after upcoming signals ceased to arrive (Fig. 6a). These reverberations retained the phase they had at that time. This effect produced mod-

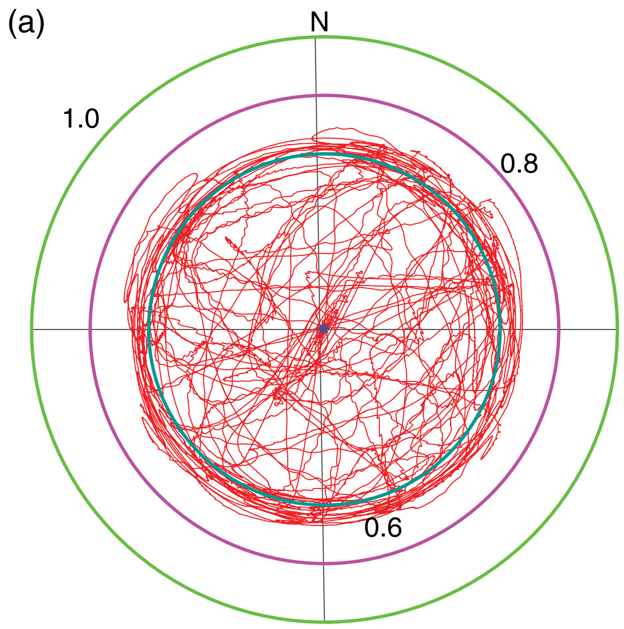

Shallow attenuation

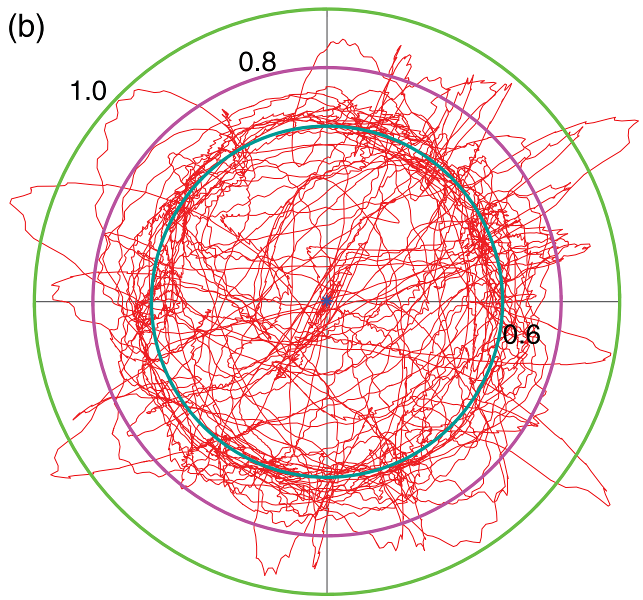

No shallow attenuation

Figure 7. Polar plots of the nonlinear layer model in Figure 6, as in Figure 2a. (a) Shallow attenuation is included. The signal is approximately bounded by a normalized acceleration of 0.7. The signal is transiently circularly polarized. (b) Shallow attenuation is turned off. High-frequency excursions occur. The jitter is 800 Hz, which was left in to show that the method is nondispersive and to provide time marks. The color version of this figure is available only in the electronic edition.

erate amplitude northeast–southwest movement visible in Figure 7a.

It is conceivable that rock cohesion and the moorings of the seismograph suppress very shallow nonlinear attenuation. Shallow muddy soils have a similar effect when the anelastic strain rate increases gradually with the resolved shear traction as discussed in the Application to Reverberating Signal within Soft Sediments section. We simply modeled shallow cohesion by turning off frictional failure arbitrarily within the uppermost 1.475 m. The quarter-wavelength frequency for this depth is 67.8 Hz. As expected, this modification allows high-frequency signal with shallow quarter-wavelength depths to reach the surface. Arrows mark strong high-frequency pulses in Figure 6b. Brief episodes of strong high-frequency acceleration are much more evident on the polar plot (Fig. 7b).

There is only weak resonance in the gradient model (Fig. 8a). The tendency for clipping from equation (10) at a resolved acceleration is evident in the polar plot (Fig. 9a). There is a tendency for transient circular polarization near the maximum resolved acceleration. We represented shallow cohesion by turning off frictional failure in the uppermost 0.0037 s of travel time from the surface, as was done in the layer model. High frequencies reach the surface as expected in the model with no shallow attenuation (Figs. 8b and 9b).

Overpressured Aquifer

Artesian aquifers existed beneath the Los Angeles basin (Mendenhall, 1905a,b,c,d, 1908; Johnson and Chong, 2005) and the Santa Clara basin (Clark, 1924; Poland and Ireland, 1988; Iwamura, 1995) during preindustrial times. Such overpressure would have reduced the frictional strength within the aquifers and suppressed impinging *S* waves. This process is potentially relevant to preindustrial earthquakes, such as the 1857 Fort Tejon event as felt in downtown Los Angeles (Agnew and Sieh, 1978). We are not aware of any relevant recording by a modern instrument above a strongly overpressured aquifer.

In principle, one might overpressure a deep aquifer to intentionally suppress impinging *S* waves. Such a societal application would need to account for detailed seismic velocity, density, and hydrological structure. Numerical hydrological models exist for the Los Angeles basin (Reichard *et al.*, 2003). Some detailed borehole information is available for the Los Angeles basin (Hayashi *et al.*, 2013) and the Santa Clara Valley (Newhouse *et al.*, 2004; O'Connell and Turner, 2011; Wentworth *et al.*, 2015). Three-dimensional numerical calculations (Roten *et al.*, 2014) would be needed to confirm that the modified fluid pressure did not inadvertently increase shaking from other types of seismic waves. Seismic hazard is already a criterion on managing groundwater in California (Metropolitan Water District of Southern California, 2007). Human activities have already increased the hazard from *S* waves in downtown Los Angeles by increasing the effective coefficient of friction in equation (6) and hence the maximum acceleration at the surface in equation (8b). The preindustrial water table was essentially at the surface and the current water table is at ~60 m depth (Johnson and Chong, 2005).

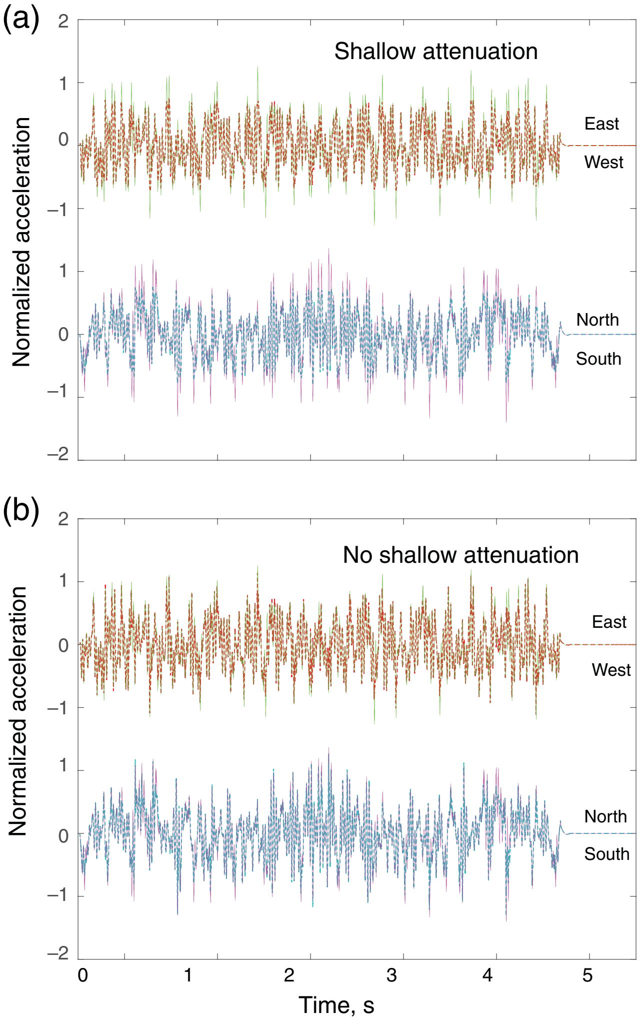

Figure 8. The normalized acceleration for the gradient model, as in Figure 6. Linear models are denoted by thin solid lines; nonlinear models are denoted by thick dashed lines. (a) The models include shallow nonlinear attenuation. There is no strong resonance. (b) Models with no shallow attenuation, high-frequency spikes are not obvious. The color version of this figure is available only in the electronic edition.

Applying simple theory, there are significant differences between deep nonlinear attenuation and nonlinear attenuation near the free surface. At depth, the scale stress is $\rho\beta|V|$, in which $|V|$ is the resolved horizontal particle velocity. For broadband signal, both the upcoming and downgoing waves contribute randomly to the particle velocity. Strong downgoing signal leads to nonlinear attenuation of the upcoming signal. The dynamic stress is higher within beds of high S-wave velocity at a given particle velocity.

We present idealized calculations to show that an overpressured aquifer has its expected effect within laterally homogeneous structure (Fig. 10). We retain the broadband signal in Figure 5. We modify the velocity structure to be crudely representative of a sedimentary basin. This layer model has 400 m/s above 9.95 m depth and 1500 m/s below that depth. We retain the density of 2250 $\mathrm{kg/m^3}$, which is appropriate for sediments. An excess artesian head of 100 m is applied between 100 and 150 m depth, so that the gradient of pore pressure in the layer is hydrostatic. The effective

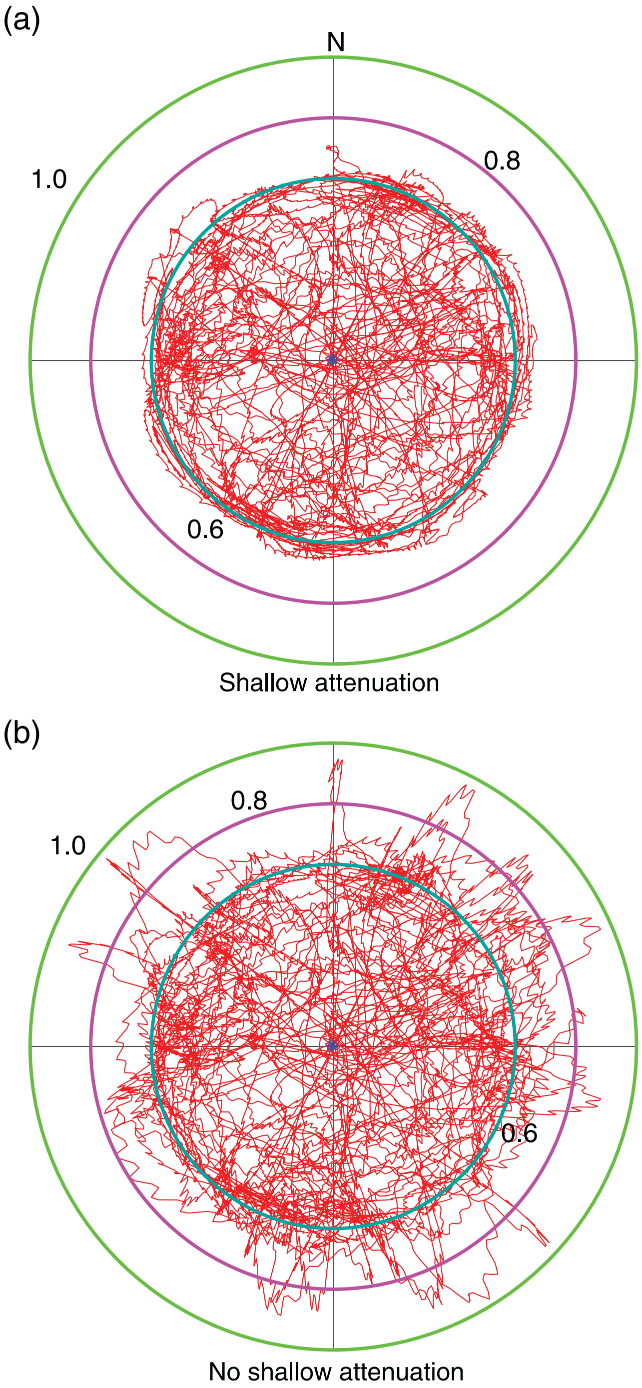

Figure 9. Polar plots of the nonlinear gradient model in Figure 8, as in Figure 7. The jitter is 800 Hz, which was left in to show that the method is nondispersive and to provide time marks. (a) Shallow attenuation is included. The signal is approximately bounded by a normalized acceleration of 0.65. The signal is transiently circularly polarized. (b) Shallow attenuation is turned off. High-frequency excursions occur. The color version of this figure is available only in the electronic edition.

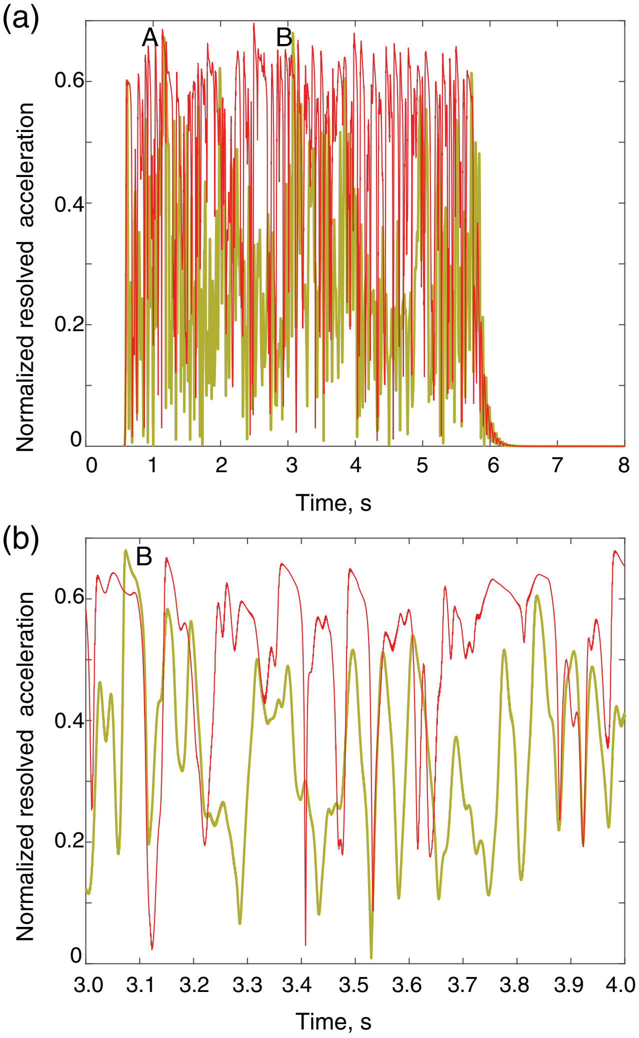

Figure 10. The normalized resolved acceleration for layer models with no fluid pressure (thin lines) and an artesian aquifer between 100 and 150 m depth (thick lines). Time origin is arbitrary. Both models include shallow nonlinear attenuation. (a) The deep aquifer generally suppresses the amplitude. High peak accelerations still occur at points A and B. The model signal without the aquifer is approximately clipped at 0.65. (b) Detail between 3 and 4 s. Signal with attenuation in the deep aquifer is not well correlated with the signal without an aquifer. The color version of this figure is available only in the electronic edition.

stress for that interval ranges between 0.24 at the top and 0.86 MPa at the bottom. The fluid pressure is zero in the rest of the model.

As expected, the resolved surface acceleration is typically less than that of a model with no fluid pressure (Fig. 10). The aquifer model signal is not simply clipped in acceleration, because the attenuation occurs well away from the free surface. Some strong acceleration pulses do occur. Unlike shallow clipping in equation (8b) with the resolved normalized acceleration at the effective coefficient of friction, the effect of the pressurized aquifer would be difficult to recognize from surface seismic records without some prior knowledge of local hydrology.

These results provide a reality check on overpressuring deep aquifers to base-isolate a city within a sedimentary basin. The excess model head of 100 m at 100 m depth brought the effective pressure down to 0.24 MPa, approximately that at 11 m depth with no water pressure. Bringing fluid pressure closer to lithostatic might trigger liquefaction in unlithified sediments. Continual pumping would be needed to maintain the fluid pressure unless elevated recharge areas exist.

Application to Reverberating Signal within Soft Sediments

Strong *S* waves reverberate within shallow compliant soil layers. Damage from nonlinear behavior may lower the *S*-wave velocity within the layer and hence the resonant frequency. Nonlinear attenuation then diminishes the amplitude of the seismic wave. The numerical methods discussed in the Appendix represent these effects and the subsequent healing of that damage once shaking has ceased. As an example application, we consider the records recorded at KiK-net station FKSH10 (latitude 37°9′30.0″ N, 140°5′46.0″ E) from the 2011 Tohoku mainshock. This station along with IBRH11, MYGH10, and TCGH16 experienced strong horizontal accelerations (Fig. 11).

The geological column at FKSH10 consists of 4 m of gravelly soil (likely human-made rubble) with an *S*-wave velocity of 150 m/s, over 4 m of gravel with an *S*-wave velocity of 650 m/s, with Quaternary and Neogene tuffaceous rocks with *S*-wave velocities of 850–1300 m/s in the rest of the hole to 203 m depth. The nominal resonance frequency is 9.375 Hz. The resonance frequency before strong shaking was ~7 Hz, indicating that the nominal structure is somewhat imprecise (Fig. 12). In addition, the dominant frequency decreased to ~5 Hz and then recovered somewhat after the shaking waned (Nakata and Snieder, 2011; Wu and Peng, 2011). This behavior occurred at other strongly shaken stations in the Tohoku mainshock (e.g., Ghofrani *et al.*, 2013). The dominant frequency for *P* waves behaved similarly (Han *et al.*, 2015). Comparison of the surface seismograms with the borehole seismograms indicates that the resonant frequency of the shallow layer in fact changed (Fig. 13c).

Analysis of low-amplitude seismograms indicates that the structure at FKSH10 is approximately laterally homogeneous (Thompson *et al.*, 2012). Thus, we make the assumption of vertical *S* waves through laterally homogeneous structure for qualitative discussion and numerical modeling. We provide caveats where appropriate. The shallow layer is likely above the water table (Han *et al.*, 2015), so liquefaction and sudden drops in fluid pressure within it are unlikely.

Qualitatively, nonlinearity during strong shaking of the soil layer modifies the surface signal from that within a linear medium in three ways. It is not *a priori* clear which effect will dominate. (1) Nonlinear attenuation directly diminishes the signal. (2) The change in the resonance peak from ~7 to

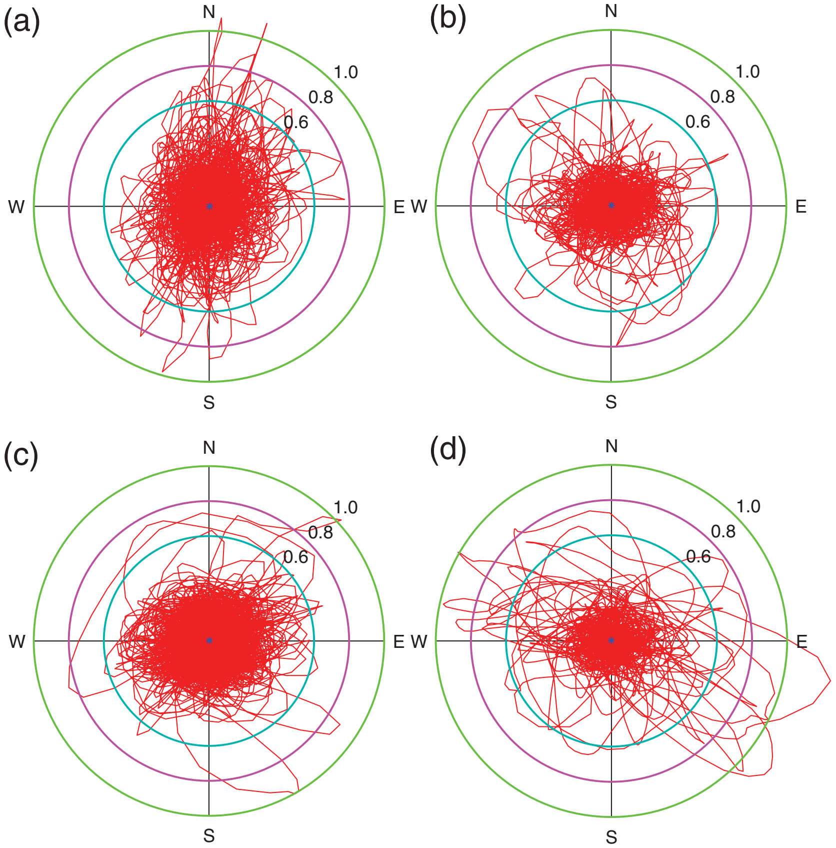

Figure 11. The normalized acceleration as in Figure 2b for the 2011 Tohoku mainshock observed at the surface at KiK-net stations: (a) FKSH10, (b) IBRH11, (c) MYGH10, and (d) TCGH16. The resolved horizontal acceleration exceeds 1g at FKSH10, MYGH10, and TCGH16. The color version of this figure is available only in the electronic edition.

~5 Hz brings the resonance into a stronger part of the spectrum for the arriving signal (Fig. 13a), which increases the surface acceleration. Physically, the signal arriving at FKSH10 is the sum of waves from numerous strong-motion generation areas on the fault plane (e.g., Joshi *et al.*, 2014; Sandeep *et al.*, 2014). The distal area on the fault plane is greater than the nearby area, so both nearby and distal regions contribute comparably. (The effect is analogous to Olbers' paradox for starlight, in which the light arriving from any one star decreases inversely with the square of its distance as r^2, but the number of stars in a spherical shell of distance r is proportional to r^2.) From a naive corner-frequency model, the upcoming acceleration spectrum in our range of interest should be approximately flat in the absence of intrinsic linear attenuation along the ray path to the borehole station. However, the borehole signal at say 3 Hz includes signals from both nearby and distal regions that are not significantly attenuated. At say 10 Hz, the distal signal is attenuated and only the nearby signal is significant. The 3 Hz signal is thus mildly stronger than the 10 Hz signal. (3) The linear resonance at 5 Hz is stronger than the resonance at 7 Hz (Fig. 14). In this model, the top layer is 4.5 m thick with an S-wave velocity of 125 or 90 m/s. The half-space velocity is 1000 m/s. The layer and half-space densities are 2000 and 2400 $\mathrm{kg/m^3}$, respectively. The resonances f are at 6.9 and 5 Hz. The amplitude decay times t_A are 0.126 and 0.231 s. The linear resonant $Q = \pi t_A f$ is 2.76 and 3.63. The ratios of surface-to-borehole acceleration allow qualitative appraisal of these effects (Fig. 13c).

First, the borehole record is only a proxy for the upcoming signal because this seismogram also includes the downgoing signal. It is in principle possible to separate upcoming and downgoing signals for a horizontally stratified linear material (e.g., Cadet *et al.*, 2012; Ghofrani *et al.*, 2013; Finn and Ruz, 2016). We attempted to use small earthquakes for which the upcoming and downgoing signals arrived separately to construct spectral transfer functions, but this method did not provide a reliable representation of the mainshock data. One reason for this is that the structure is not precisely laterally homogeneous. The spectral-ratio method in Figure 13c should remove source effects and path effects on the borehole station. The overtones are then predicted to have the same amplitudes as the primaries. The observed overtones are much less, indicating that the structure is locally homogenous on the ~4 m quarter-wavelength of the primary, but heterogeneous on the $4/3 = 1.33$ m quarter-wavelength of the overtone.

It is in principle possible to use small aftershocks and foreshocks and the concept of numerous strong-motion generation areas on the fault plane of the mainshock to disentangle the arriving signal from many directions and the shallow structure (e.g., Joshi *et al.*, 2014; Sandeep *et al.*, 2014; Otarola and Ruiz, 2016). Then, it might be feasible but difficult to iterate for sources and shallow structures including the transient effects of nonlinearity. Our calculations illustrate features that would need to be present in a 3D numerical model local to the station.

Continuing qualitatively, spectral ratios adjust for the effect that the arriving 5 Hz signal was stronger than the arriving 7 Hz in Figure 13b. Thus, they provide information on the relative importance of nonlinear attenuation and resonance. The peak of the spectral ratio is centered at ~7 Hz before strong shaking started (Fig. 13c). This observation constrains the initial linear properties of the resonance of the model in Figure 14. The peak frequency during strong shaking is ~5 Hz. The amplification at this peak should be increased above that of the 7 Hz resonance by the stronger linear amplification in Figure 14 but decreased by nonlinear

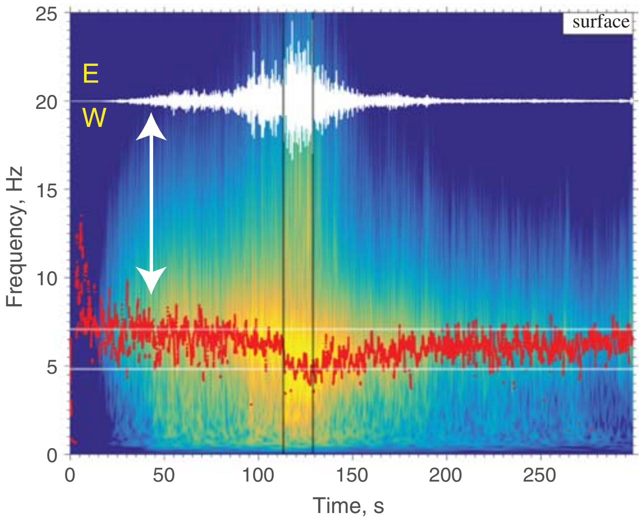

Figure 12. Frequency changes at the FKSH10 surface station during the Tohoku mainshock. The resolved horizontal spectral amplitude (background image) is the square root of the sum of the squares N–S and E–W components. The thick line indicates frequencies at the maximum spectral amplitude. The surface E–W seismogram for the Tohoku mainshock at FKSH10 is shown for reference. The arrow indicates the approximate time in which the peak frequency started to decrease. Horizontal 7 and 4.8 Hz lines are shown for reference. Vertical lines indicate the duration of strong shaking. The dominant frequency began to recover toward its previous value once strong shaking ceased. The color version of this figure is available only in the electronic edition.

attenuation. The effects approximately cancel, because both amplifications are similar. The peak after strong shaking is at ~6 Hz (indicating healing is already underway). Nonlinear attenuation should be much weaker than at peak shaking and the observed amplification is a proxy for that of a linear resonance. As expected from the linear model in Figure 14, the 6 Hz amplification is greater than the 7 Hz amplification. The observed 6 Hz amplification is also greater than the 5 Hz amplification unlike the linear prediction. This is further evidence that nonlinear attenuation suppressed amplification of the 5 Hz resonance during the strongest shaking.

We continue with a feature of the record that is evident in the time domain. The horizontal PGA approaches and even exceeds to 1*g* in the stations in Figure 11. This observation is not expected from equation (8b) in the normalized acceleration and should not exceed the intrinsic coefficient of friction above the water table. An exceptionally large coefficient of friction for the soil layer at FKSH10 is unlikely. The soil began to fail with damage at a modest acceleration (Fig. 12). The same reasoning applies to the possibility of very cohesive soil.

Most likely the soil behaved as a mildly nonlinear substance rather than as a plastic or frictional material in which strain rate increases rapidly with stress (Fig. 15). A mixture of soft clay and gravel might have a viscous Bingham rheology. The gravel grains lock at small stresses but slide over each other at a constant stress above a threshold once their friction is overcome. The clay supports an increasing fraction of the macroscopic stress as it deforms viscously at high strain rates. At a microscopic level, frictional sliding of gravel occurs at real contacts that cover a small part of the macroscopic surface area. Real stresses are a few gigapascals in which strain rate depends exponentially on contact shear traction. Real stresses in the soft clay are low, the real contact area is high, and strain rate depends mildly on stress.

We used the numerical code in the Appendix to calculate an example model based on the nominal properties of FKSH10 to illustrate features that are visible in the time domain. A 3.915-m thick layer with an *S*-wave velocity of 150 m/s overlies a half-space with a velocity of 1000 m/s. The density is 2250 $\mathrm{kg/m^3}$. Numerically, the grid spacing in the layer is 0.03 m; the time step is 0.2 ms. The frictional failure properties of the half-space are modified from the previous models so that little nonlinear attenuation occurs in that region; the half-space parameters used in the Appendix are $m = 5$, $\mu_M = 0.9$, $\zeta = 1$, and $\mu_B = 0.4$. The anelastic strain rate increases slowly with resolved shear traction in the soil layer (Fig. 15); the soil layer parameters are $m = 2$, $\mu_M = 0.9$, $\zeta = 0.001$, and $\mu_B = 0.1$.

The change in the shear modulus during a time step in the soil is assumed to be

$$\Delta G = G\left[1 - \Lambda|\Delta\varepsilon| + H\left(\frac{G_0 - G}{G_0}\right)^3\right], \tag{13}$$

in which the dimensionless coefficient Λ is 37, the dimensionless coefficient H is 2×10^{-4}, $\Delta\varepsilon$ is the additional resolved horizontal strain in the time step, and G_0 is the original elastic shear modulus. We calibrated our coefficients to provide results similar to observations, in which the calculated elastic and nonlinear accelerations are similar. The form of equation (13) is arbitrary, but does have some intuitive aspects. (1) The shear modulus cannot go to zero or become negative. (2) The relative rate of change of the shear modulus is linearly proportional to the anelastic strain rate. (3) The shear modulus heals toward its original value. Our method is not intended to represent the long-term evolution of the shear modulus, only evolution during and immediately after shaking. (4) The shear modulus heals rapidly when it is much less than the original shear modulus.

We obtained our assumed upcoming signal by repeating the signal used in the main article to obtain an ~13-s time series (Fig. 16). The broadband spectra are similar to the observed borehole spectrum (Fig. 12). It was not tractable to have a long duration of weak signal before and after the strong signal as in the real record (Fig. 12).

The computed surface acceleration (Fig. 17) exhibits the expected properties. The resonant frequency of the nonlinear signal progressively became lower as damage reduced the shear modulus of the layer. The nonlinear

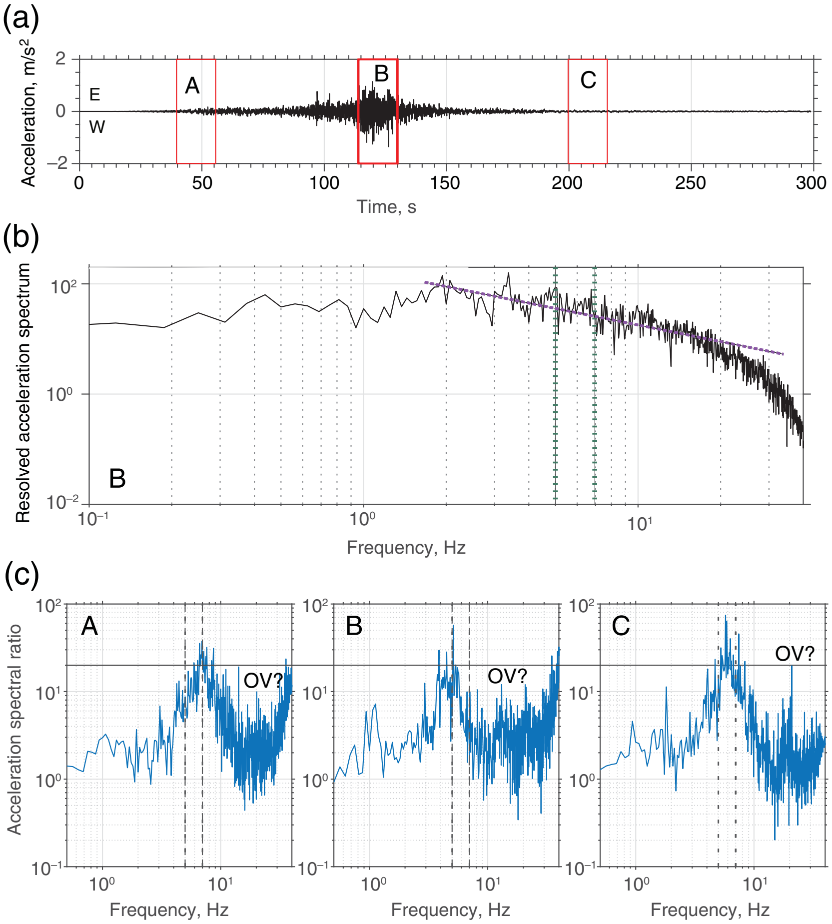

Figure 13. (a) The E–W acceleration recorded in the borehole station at FKSH10. The surface acceleration in a linear half-space would be approximately twice the recorded value and less than $0.2g$, but this is not the case owing to near-surface amplification. Signals obtained from time windows A, B, and C are processed in (b) and (c). (b) The borehole acceleration is the square root sum of the squares of the E–W and N–S components for strong shaking in time window B. A slope of 1 in the log–log scale is shown in the region of interest for reference. (c) Spectral ratios of surface to borehole for resolved spectra from time windows A, B, and C. Damage within the soil layer moved the spectral peak from ~7 Hz in window A to ~5 Hz in window B. The peak recovered to ~6 Hz in window C. Marginally resolved overtones (OV?) should have three times the fundamental frequency and the same amplitude as the fundamental for an elastic layer over a half-space. The observed amplitude, however, is much less than as predicted. The color version of this figure is available only in the electronic edition.

signal is stronger than the reference linear signal at times. That is, the combined effects of stronger resonance and stochastically stronger signal at the lower resonant frequency overcame the direct effect of increased attenuation. The resonant period dominates, so the computed signals of the linear and nonlinear time series in Figure 17b look quite different. The computed absolute acceleration approached $1g$ (Fig. 18).

The computed change in the shear modulus increased rapidly with time at the start of strong shaking (Fig. 19a). The rate of modulus change decreased as healing became important. The curve is irregular because some healing occurred at times of low resolved shear traction and low anelastic strain rate. Damage and healing did not come to equilibrium in this calculation, as would occur if the positive and negative terms in equation (13) offset each other. It is not clear whether this equilibrium occurred in the real data in Figure 12, because one cannot finely resolve resonant frequency over small time windows.

The computed damage was concentrated in the lower part of the layer (Fig. 19b). Physically, dynamic stresses and, hence, dynamic strain rates, are small near the free surface. As a matter of interpretation, it is then difficult to tell whether the real nonlinear behavior depended on the coulomb stress ratio, because the normal traction did not vary a lot over the lowermost 2 m of the soil layer. The borehole and surface stations are too far apart (203 m) to resolve the detailed structure of the soil layer. The ~$1g$ bound on acceleration in Figure 11 from equation (8b) shows that a coulomb-based failure criterion may be relevant.

Conclusions

Our basic testable assumption is that coulomb friction provides a reasonable representation of failure of the shallow subsurface from strong S waves. The shear traction on horizontal planes depends on the product of the elastic strain and the shear modulus. A flow law represents the anelastic strain rate, which increases rapidly with resolved horizontal shear traction. This construct differs from the widely used Masing rules that represent strain as a function of stress.

Simple scaling relationships arise for the predicted signal in the time domain that would be cloaked by a purely spectral treatment. The resolved horizontal acceleration normalized to the acceleration of gravity is bounded by the effective coefficient of friction in equation (8b). This feature may be seen with real data by plotting (A_x, A_y) or resolved acceleration versus time (Fig. 2). In more detail, very shallow cohesion increases the maximum acceleration amplitude at high frequencies. Such arrivals are not harbingers of sustained (lower frequency) horizontal accelerations above $1g$ in future events. Numerical calculations confirmed these expected features and are intended as a guide to fully 3D calculations (Roten *et al.*, 2014) in which real seismograms are available and the near-surface structure is well constrained. Analyti-

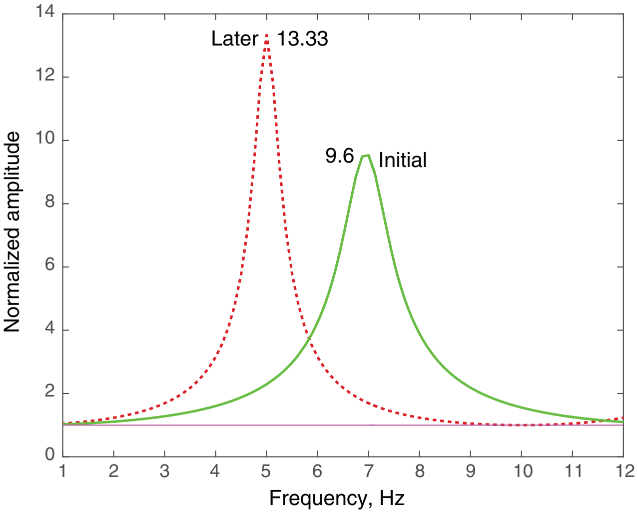

Figure 14. The computed surface amplitudes above a linear layer over a half-space are normalized to the amplitude that would be observed at the surface of a half-space. The model simply represents the subsurface at FKSH10. Before shaking, the resonant period is 7 Hz. Damage from strong shaking decreased the *S*-wave velocity in the layer. The resonant frequency decreased to ~5 Hz. The peak amplification factor increased to 13.33. The color version of this figure is available only in the electronic edition.

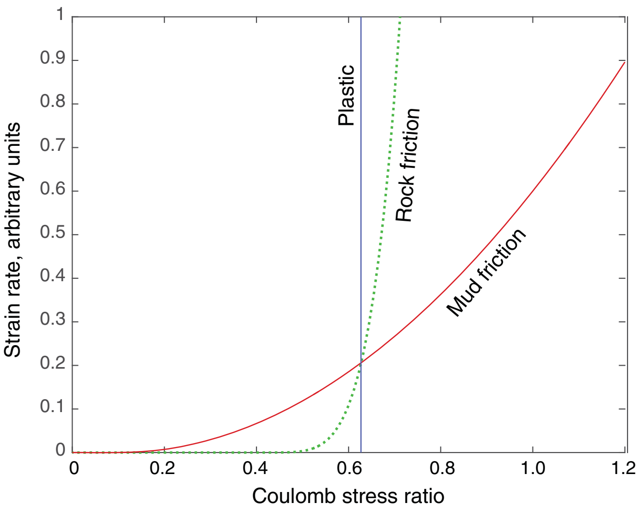

Figure 15. Strain rate versus coulomb stress ratio for possible rheologies. The plastic strain rate (vertical line) goes from extremely slow to very fast when the failure stress is reached. The assumed strain rate for rock friction in the Appendix (dashed curve) increases rapidly with stress. The assumed strain for mud friction (solid curve) increases gradually with stress. The color version of this figure is available only in the electronic edition.

cally, other deviatoric stresses, as from the near-field velocity pulse and surface waves, decrease the maximum resolved acceleration.

Numerical calculations illustrated other expected features of frictional attenuation that are predicted to occur on real seismograms. (1) There is a tendency for strong signal to become transiently circularly polarized near the maximum resolved acceleration. Higher frequency signal perpendicular to the ambient acceleration does not add greatly to the resolved acceleration and is thus not suppressed. There are not enough excursions to high amplitude in the Lucerne data in Figure 2a to perform a meaningful statistical test (see McKinnon, 2002) for transient circular polarization. (2) Unlike ordinary attenuation, frictional attenuation does not preferentially suppress high frequencies. A high-frequency signal on one horizontal component that adds to the resolved acceleration also increases the attenuation of the other component, even if it is initially free of high frequencies. An equivalent linear model would not resolve either effect.

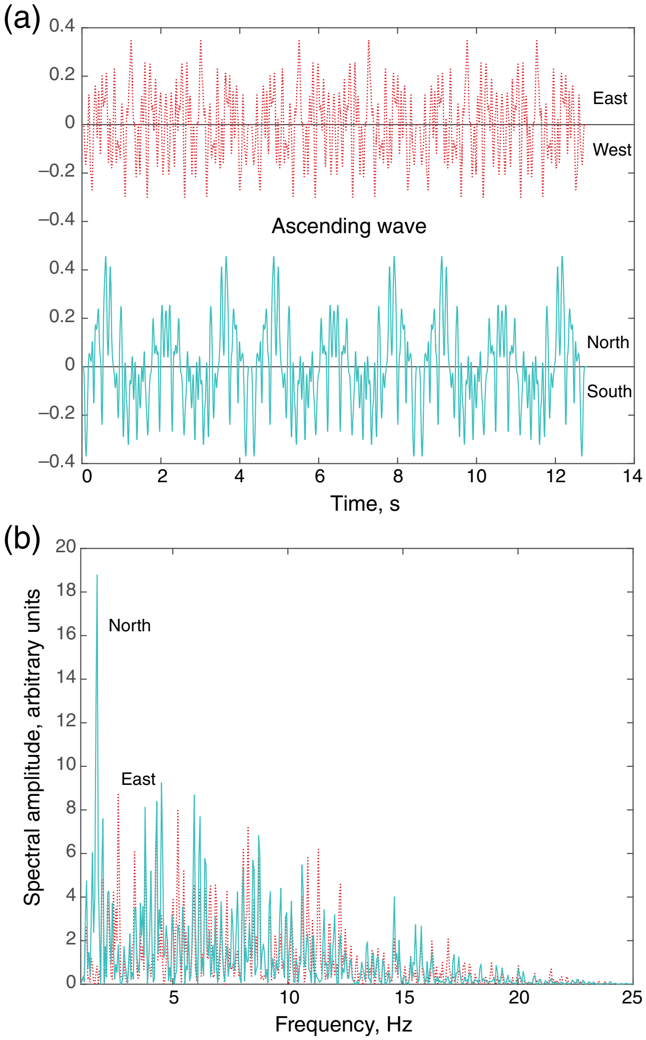

Figure 16. (a) The assumed upcoming signal on the E–W (dashed) and N–S (solid) components is normalized to the surface amplitude in an elastic half-space. Zero time is the start of the signal. (b) The assumed spectral amplitudes. The color version of this figure is available only in the electronic edition.

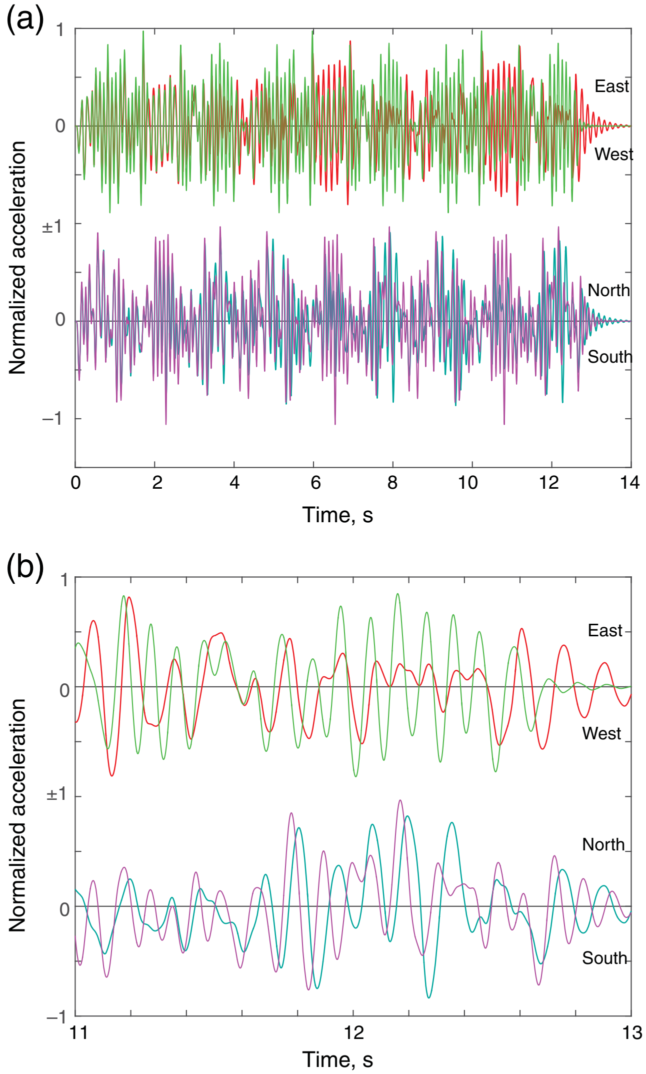

Figure 17. Model surface seismogram with nonlinear model (thick curves) and linear model (thin curves). Zero time is start of shaking. (a) The full duration of strong shaking. (b) The signal windowed between 11 and 13 s. The computed nonlinear signal is not obviously similar to the linear signal. The resonant frequency of the nonlinear model decreased modestly over the full interval. The adjacent peaks of the linear model are typically closer than those of the nonlinear model. The color version of this figure is available only in the electronic edition.

As an application, frictional attenuation within a deep overpressured aquifer does suppress signal at the surface. The effect, however, is complicated because upcoming and downgoing waves interact. The predicted surface signal does not clip at a given acceleration. Again, the constructs of PGA and damping factor provide an incomplete description.

In another application, surface accelerations above 1g can occur above a shallow layer of compliant soil. The resonant frequency of the layer then decreases as damage reduces its S-wave velocity. The layer begins to heal once strong shaking ceases. The high-frequency accelerations can occur because the anelastic strain rate in the ductile layer increases slowly with dynamic shear traction, so scaling relationship (8b) that the coulomb stress ratio is proportional to the acceleration in g's does not imply a sharp limit on acceleration. Still anelastic strain precludes much larger accelerations. Observation of such rogue accelerations (Fig. 11) is thus not a harbinger of future extreme accelerations.

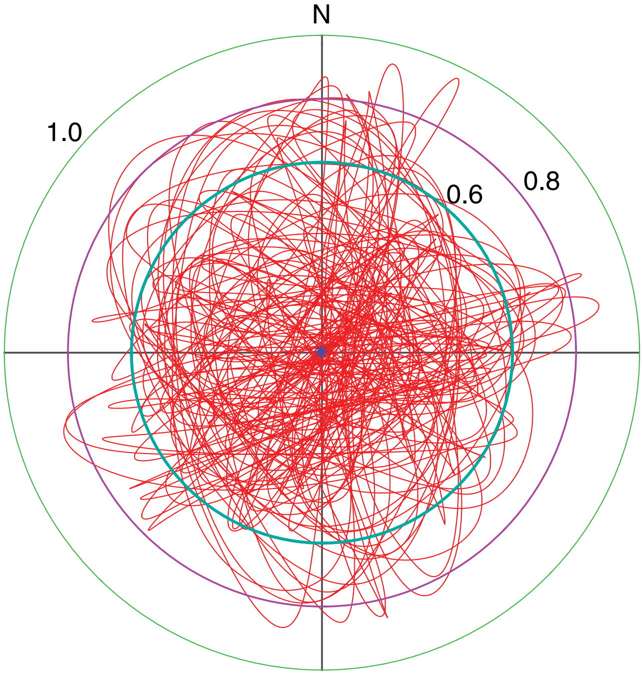

Figure 18. Polar plot of horizontal acceleration as in Figure 11. The maximum acceleration approaches 1g. The color version of this figure is available only in the electronic edition.

Data and Resources

Corrected horizontal Lucerne records were provided in text format by Consortium of Organizations for Strong Motion Observation Systems (COSMOS) Virtual Data Center. They are available upon request from that source. Japanese seismograms and subsurface station information are publically available from the National Research Institute for Earth Science and Disaster Resilience in Japan. The rest of the data used in this article came from published sources listed in the References. We used the white noise function "wgn" in Matlab version R2015b to generate random time series. It is available commercially from www.mathworks.com/products/matlab (last accessed May 2016).

Acknowledgments

Domniki Asimiki, Bo Han, Ralph Archuleta, Fabian Bonilla, and William Ellsworth answered our queries. Two anonymous reviewers provided helpful comments. This research was supported by the Southern California Earthquake Center (SCEC). SCEC is funded by National Science Foundation (NSF) Cooperative Agreement EAR-0106924 and U.S. Geological Survey (USGS) Cooperative Agreement 02HQAG0008. The SCEC Contribution Number for this article is 7204.

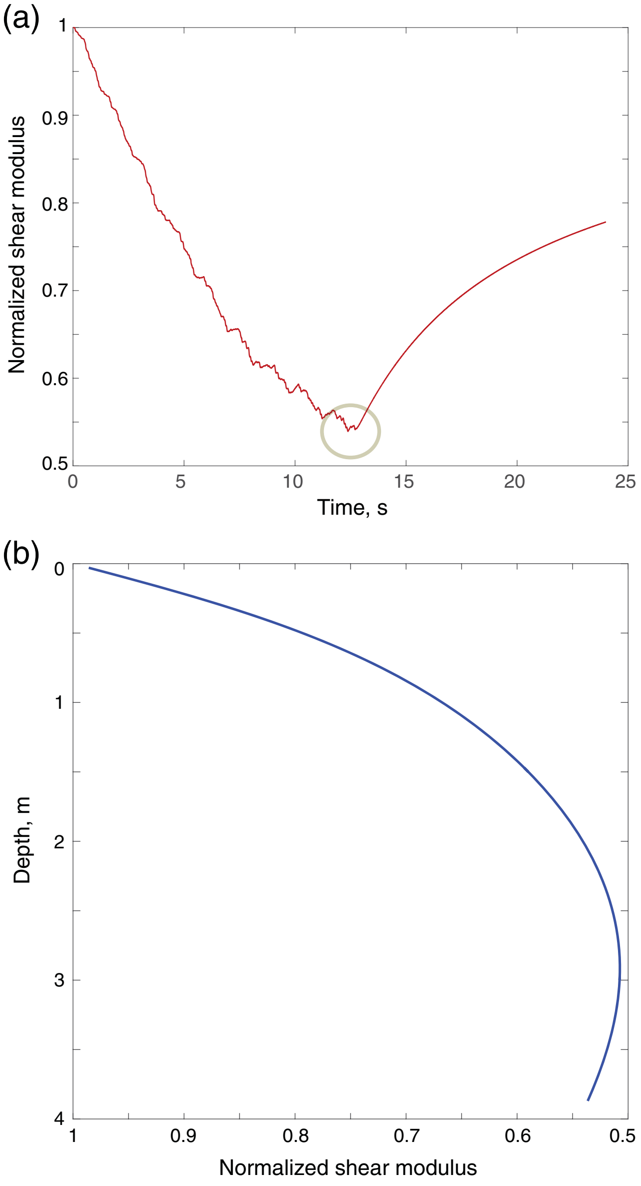

Figure 19. The shear modulus is normalized to the modulus starting G_0 within the soil layer. (a) The time history of the modulus at 1.875 m depth. The modulus recovered slightly during brief intervals of weak resolved shear traction. The modulus recovered smoothly once the shaking ceased. The modulus at the end of strong shaking did not come into equilibrium. The descending and ascending curves (within ellipse) meet at an angle. It is clear whether the real data in Figure 12 have the latter property. (b) The depth distribution of damage at the end of strong shaking. Damage is concentrated toward the base of the layer. The color version of this figure is available only in the electronic edition.

References

Afshari, K., and J. P. Stewart (2015). Effectiveness of 1D ground response analyses at predicting site response at California vertical array sites, *Proc. SMIP2015 Seminar on Utilization of Strong Motion Data, California Strong Motion Instrumentation Program*, Sacramento, California, 22 October 2015, 23–40.

Afshari, K., and J. P. Stewart (2016). Physically parameterized prediction equations for significant duration in active crustal regions, *Earthq. Spectra* **32,** no. 4, 2057–2081, doi: 10.1193/063015EQS106M.

Agnew, D. A., and K. E. Sieh (1978). A documentary study of the felt effects of the Great California earthquake of 1857, *Bull. Seismol. Soc. Am.* **68,** 1717–1729.

Aoi, S., T. Kunugi, and H. Fujiwara (2008). Trampoline effect in extreme ground motions, *Science* **332,** 727–730.

Assimaki, D., W. Li, and A. Kalos (2011). A wavelet-based seismogram inversion algorithm for the in situ characterization of nonlinear soil behavior, *Pure Appl. Geophys.* **168,** 1669–1691, doi: 10.1007/s00024-010-0198-6.

Assimiki, D., W. Li, J. H. Steidl, and J. Schmedes (2008). Quantifying nonlinearity susceptibility via site-response modeling uncertainty at three sites in the Los Angeles basin, *Bull. Seismol. Soc. Am.* **98,** no. 5, 2364–2390.

Barbot, S., and Y. Fialko (2010). A unified continuum representation of post-seismic relaxation mechanisms: Semi-analytic models of after-slip, poroelastic rebound and viscoelastic flow, *Geophys. J. Int.* **182,** 1124–1140.

Bonilla, L. F., K. Tsuda, N. Pulido, J. Régnier, and A. Laurendeau (2011). Nonlinear site response evidence of K-NET and KiK-net records from the 2011 off the Pacific coast of Tohoku earthquake, *Earth Planets Space* **63,** 785–789.

Byerlee, J. (1978). Friction in rocks, *Pure Appl. Geophys.* **116,** 616–626.

Cadet, H., P.-Y. Bard, and A. Rodriguez-Marek (2012). Site effect assessment using KiK-net data: Part 1. A simple correction procedure for surface/downhole spectral ratios, *Bull. Earthq. Eng.* **10,** no. 2, 421–448.

Chen, X. (1995). Near-field ground motion from the Landers earthquake, *Ph.D. Thesis*, California Institute of Technology, Pasadena, California, 147 pp.

Clark, W. O. (1924). Ground water in Santa Clara Valley, California, *U.S. Geol. Surv. Water-Supply Pap. 519*, 209 pp.

Dieterich, J. H. (1979). Modeling of rock friction: 1. Experimental results and constitutive equations, *J. Geophys. Res.* **84,** no. B5, 2161–2168.

Drucker, D. C., and W. Prager (1952). Soil mechanics and plastic analysis for limit design, *Q. Appl. Math.* **10,** 157–165.

Finn, W. D. L., and F. Ruz (2016). Amplification effects of thin soft surface layers, *Earthq. Spectra* **32,** no. 4, 2109–2126.

Fischer, A. D., and C. G. Sammis (2009). Dynamic driving of small shallow events during strong motion, *Bull. Seismol. Soc. Am.* **99,** 1720–1729.

Fischer, A. D., Z. G. Peng, and C. G. Sammis (2008). Dynamic triggering of high-frequency bursts by strong motions during the 2004 Parkfield earthquake sequence, *Geophys. Res. Lett.* **35,** L12305, doi: 10.1029/2008GL033905.

Fischer, A. D., C. G. Sammis, Y. L. Chen, and T.-L. Teng (2008). Dynamic triggering by strong motion *P*- and *S*-waves: Evidence from 1999 Chi-Chi, Taiwan earthquake, *Bull. Seismol. Soc. Am.* **98,** 580–592.

Ghofrani, H., G. M. Atkinson, and K. Goda (2013). Implications of the 2011 M 9.0 Tohoku Japan earthquake for the treatment of site effects in large earthquakes, *Bull. Earthq. Eng.* **11,** 171–203.

Groholski, D. R., Y. M. A. Hashash, B. Kim, M. Musgrove, J. Harmon, and J. P. Stewart (2016). Simplified model for small-strain nonlinearity and strength in 1D seismic site response analysis, *J. Geotech. Geoenvir. Eng.* **142,** no. 9, doi: 10.1061/(ASCE)GT.1943-5606.0001496.

Han, B., Z. Yang, L. Zdravković, and S. Kontoe (2015). Non-linearity of gravelly soils under seismic compressional deformation based on KiK-net downhole array observations, *Géotech. Lett.* **5,** 287–293, doi: 10.1680/jgele.15.00130.

Hartzell, S. H., L. F. Bonilla, and R. A. Williams (2004). Prediction of nonlinear soil effects, *Bull. Seismol. Soc. Am.* **94,** no. 5, 1609–1629.

Hayashi, K., A. Martin, K. Hatayama, and T. Kobayashi (2013). Estimating deep S-wave velocity structure in the Los Angeles basin using a passive surface-wave method, *The Leading Edge* **32,** 620–626.

Ikari, M. J., D. M. Saffer, and C. Marone (2009). Frictional and hydrologic properties of clay-rich fault gouge, *J. Geophys. Res.* **114,** no. B05409, doi: 10.1029/2008JB006089.

Iwamura, T. I. (1995). Hydrogeology of the Santa Clara and Coyote Valleys groundwater basins, California, in *Recent Geologic Studies in the San Francisco Bay Area: SEPM (Society for Sedimentary Geology), Pacific Section*, E. S. Sangines, D. A. Anderson, and A. V. Busing (Editors), Pac. Sect., Soc. of Econ. Paleontol. and Mineral., Santa Barbara, California, Vol. 76, 173–192.

Iwan, W. D., and X. Chen (1995). Important near-field ground motion data from the Landers earthquake, *10th European Conf. on Earthquake Engineering*, G. Duma (Editor), Balkema, Rotterdam, The Netherlands, 229–234.

Johnson, T., and B. Chong (2005). *A Century of Groundwater Changes in the Central and West Coast Basins*, Water Replenishment District of Southern California, Technical Bulletin, Lakewood, California, Vol. 4, summer, 2 pp.

Joshi, A., Sandeep, and Kamal (2014). Modeling of strong motion generation areas of the 2011 Tohoku, Japan earthquake using modified semi-empirical technique, *Nat. Hazard* **71,** 587–609.

Kaklamanos, J., L. G. Baise, E. M. Thompson, and L. Dorfmann (2015). Comparison of 1D linear, equivalent-linear, and nonlinear site response models at six KiK-net validation sites, *Soil Dynam. Earthq. Eng.* **69,** 207–219.

Kausel, E., and D. Assimaki (2002). Seismic simulation of inelastic soils via frequency-dependent moduli and damping, *J. Eng. Mech.* **128,** 34–47.

Kohli, A. H., and M. D. Zoback (2013). Frictional properties of shale reservoir rocks, *J. Geophys. Res.* **118,** 5109–5125, doi: 10.1002/jgrb.50346.

Lavallée, D., and R. J. Archuleta (2005). Coupling of the random properties of the source and the ground motion for the 1999 Chi Chi earthquake, *Geophys. Res. Lett.* **32,** L08311, doi: 10.1029/2004GL022202.

Linker, M. F., and J. H. Dieterich (1992). Effects of variable normal stress on rock friction: Observations and constitutive equations, *J. Geophys. Res.* **97,** 4923–4940.

Marsan, D. (2005). The role of small earthquakes in redistributing crustal elastic stress, *Geophys. J. Int.* **163,** 141–151.

McKinnon, M. M. (2002). Statistical modeling of the circular polarization in pulsar radio emission and detection statistics of radio polarimetry, *Astrophys. J.* **568,** 302–311.

Mendenhall, W. C. (1905a). Development of underground waters in the central coastal plain region of southern California, *U.S. Geol. Surv. Water-Supply Irrig. Pap. 138*, 162 pp.

Mendenhall, W. C. (1905b). Development of underground waters in the western coastal plain region of southern California, *U.S. Geol. Surv. Water-Supply Irrig. Pap. 139*, 103 pp.

Mendenhall, W. C. (1905c). Development of underground waters in the eastern coastal plain region of southern California, *U.S. Geol. Surv. Water-Supply Irrig. Pap. 137*, 140 pp.

Mendenhall, W. C. (1905d). The hydrology of San Bernadino Valley, California, *U.S. Geol. Surv. Water-Supply Irrig. Pap. 142*, 124 pp.

Mendenhall, W. C. (1908). Ground waters and irrigation enterprises in the foothill belt of southern California, *U.S. Geol. Surv. Water-Supply 219*, 175 pp.

Metropolitan Water District of Southern California (2007). Chapter IV—Groundwater basin reports San Fernando Valley basins—Upper Los Angeles River area basins, *Final Groundwater Assessment Study A Status Report on the Use of Groundwater in the Service Area of the Metropolitan Water District of Southern California Report Number 1308*, IV-2-1–IV-2-19.

Nakata, N., and R. Snieder (2011). Near-surface weakening in Japan after the 2011 Tohoku-Oki earthquake, *Geophys. Res. Lett.* **38,** L17302, doi: 10.1029/2011GL048800.

Newhouse, M. W., R. T. Hanson, C. M. Wentworth, R. R. Everett, C. F. Williams, J. C. Tinsley, T. E. Noce, and B. A. Carkin (2004). Geologic, water-chemistry, and hydrologic data from multiple-well monitoring sites and selected water-supply wells in the Santa Clara Valley, California, 1999–2003, *U.S. Geol. Surv. Sci. Invest. Rept. 2004-5250*, 134 pp.

O'Connell, D. R. H., and J. P. Turner (2011). Interferometric multichannel analysis of surface waves (IMASW), *Bull. Seismol. Soc. Am.* **101,** 2122–2141.

Otarola, C., and S. Ruiz (2016). Stochastic generation of accelerograms for subduction earthquakes, *Bull. Seismol. Soc. Am.* **106,** no. 6, doi: 10.1785/0120150262.

Perfettini, H., J. Schmittbuhl, J. R. Rice, and M. Cocco (2001). Frictional response induced by time-dependent fluctuations of the normal load, *J. Geophys. Res.* **106,** no. B7, 13,455–13,472.

Petrovic, B., and S. Parolai (2016). Joint deconvolution of building and downhole strong-motion recordings: Evidence for the seismic wavefield being radiated back into the shallow geological layers, *Bull. Seismol. Soc. Am.* **106,** no. 4, 1720–1732, doi: 10.1785/0120150326.

Phillips, C., and Y. M. A. Hashash (2009). Damping formulation for nonlinear 1D site response analyses, *Soil Dynam. Earthq. Eng.* **29,** 1143–1158.

Poland, J. F., and R. L. Ireland (1988). Land subsidence in the Santa Clara Valley, California, as of 1982, *U.S. Geol. Surv. Profess. Pap. 497-F*, 61 pp.

Reichard, E. G., M. Land, S. M. Crawford, T. Johnson, R. R. Everett, T. V. Kulshan, D. J. Ponti, K. J. Halford, T. A. Johnson, K. S. Paybins, *et al.* (2003). Geohydrology, geochemistry, and ground-water simulation-optimization of the Central and West Coast basins, Los Angeles County, California, *U.S. Geol. Surv. Water-Res. Invest. Rept. 03-4065*, 184 pp.

Roten, D., K. B. Olsen, S. Day, Y. Cui, and D. Fäh (2014). Expected seismic shaking in Los Angeles reduced by San Andreas fault zone plasticity, *Geophys. Res. Lett.* **41,** 2769–2777, doi: 10.1002/2014GL059411.

Rubinstein, J. L., and G. C. Beroza (2004). Nonlinear strong ground motion in the M_L 5.4 Chittenden earthquake: Evidence that preexisting damage increases susceptibility to further damage, *Geophys. Res. Lett.* **31,** L23614, doi: 10.1029/2004GL021357.

Ruina, A. (1983). Slip instability and state variable laws, *J. Geophys. Res.* **88,** no. B12, 10,359–10,370.

Sandeep, A. Joshi, Kamal, P. Kumar, and A. Kumar (2014). Effect of frequency-dependent radiation pattern in the strong motion simulation of the 2011 Tohoku earthquake, Japan, using modified semi-empirical method, *Nat. Hazards* **73,** 1499–1521, doi: 10.1007/s11069-014-1153-0.

Santisi d'Avila, M. P., L. Lenti, and J.-F. Semblat (2012). Modelling strong seismic ground motion: Three-dimensional loading path versus wavefield polarization, *Geophys. J. Int.* **90,** no. 3, 1607–1624, doi: 10.1111/j.1365-246X.2012.05599.x.

Sleep, N. H. (1998). Rake dependent rate and state friction, *J. Geophys. Res.* **103,** no. B4, 7111–7119, doi: 10.1029/98JB00199.

Sleep, N. H. (2010). Strong seismic shaking of randomly prestressed brittle rocks, rock damage, and nonlinear attenuation, *Geochem. Geophys. Geosys.* **11,** Q10002, doi: 10.1029/2010GC003229.

Sleep, N. H. (2012). Site resonance from strong ground motions at Lucerne, California, during the 1992 Landers mainshock, *Bull. Seismol. Soc. Am.* **102,** 1505–1513.

Sleep, N. H., and B. A. Erickson (2014). Nonlinear attenuation of S-waves and Love waves within ambient rock, *Geochem. Geophys. Geosys.* **15,** 1419–1440, doi: 10.1002/2014GC005250.

Sleep, N. H., and S. Ma (2008). Production of brief extreme ground acceleration pulses by nonlinear mechanisms in the shallow subsurface, *Geochem. Geophys. Geosys.* **9,** Q03008, doi: 10.1029/2007GC001863.

Sleep, N. H., and N. Nakata (2015). Nonlinear attenuation from the interaction between different types of seismic waves and interaction of seismic waves with shallow ambient tectonic stress, *Geochem. Geophys. Geosys.* **16,** 2336–2363, doi: 10.1002/2015GC005832.

Sleep, N. H., and N. Nakata (2016). Nonlinear suppression of high-frequency S waves by strong Rayleigh waves, *Bull. Seismol. Soc. Am.* **106,** no. 5, 2302–2312.

Stewart, J. P., J. Douglas, M. Javanbarg, Y. Bozorgnia, N. A. Abrahamson, D. M. Boore, K. W. Campbell, E. Delavaud, M. Erdik, and P. J. Stafford (2015). Selection of ground motion prediction equations for the global earthquake model, *Earthq. Spectra* **31,** no. 1, 19–45.

Thompson, E. M., L. G. Baise, Y. Tanaka, and R. E. Kayen (2012). A taxonomy of site response complexity, *Soil Dynam. Earthq. Eng.* **41,** 32–43.

Tobita, T., S. Iai, and T. Iwata (2010). Numerical analysis of near-field asymmetric vertical motion, *Bull. Seismol. Soc. Am.* **100,** no. 4, 1456–1469

Wang, J., C. Xu, J. T. Freymueller, Z. Li, and W. Shen (2014). Sensitivity of Coulomb stress change to the parameters of the Coulomb failure model: A case study using the 2008 M_w 7.9 Wenchuan earthquake, *J. Geophys. Res.* **119,** 3371–3392, doi: 10.1002/2012JB009860.

Wentworth, C. M., R. C. Jachens, R. A. Williams, J. C. Tinsley, and R. T. Hanson (2015). Physical subdivision and description of the water-bearing sediments of the Santa Clara Valley, California, *U.S. Geol. Surv. Sci. Invest. Rept. 2015-5017*, 73 pp.

Wu, C., and Z. Peng (2011). Temporal changes of site response during the 2011 M_w 9.0 off the Pacific coast of Tohoku earthquake, *Earth Planets Space* **63,** 791–795.

Zalachoris, G., and E. M. Rathje (2015). Evaluation of one-dimensional site response techniques using borehole arrays, *J. Geotech. Geoenvir. Eng.* **141,** no. 12, 04015053.

Appendix

Numerical Model

Our tractable numerical method follows those of Sleep and Erickson (2014) and Sleep and Nakata (2015). We numerically evaluate the time history (in steps of Δt) of ground motions and anelastic strains from vertical S waves in two horizontal dimensions. We modify the code to allow the shear modulus, the coefficient of friction, and fluid pressure to vary with depth. The density remains constant with depth at 2250 kg/m^3.

The method is essentially finite difference with some aspects of finite elements over depth intervals. We use staggered elements and nodes. The shear traction, elastic strain, and anelastic strain nodes are evaluated at nodes at the center of elements. The shear modulus, the coefficient of friction, the shear-wave velocity β, and the effective pressure are constant within these elements. The depth range of elements is $\Delta Z = \beta \Delta t$; the code remains stable but becomes mildly dispersive if $\beta \Delta t$ is less than the depth interval. Displacement, velocity, acceleration, and the density for the momentum equation (2) are evaluated at intermediate nodes at the boundaries of the strain elements. The shear traction and anelastic strain are zero at the free surface, the location of the shallowest strain node. The surface acceleration is hence evaluated at the very shallow depth of $\beta \Delta t/2$, 0.05 and 0.015 m in the models.

The initial anelastic strains, displacements, velocities, and accelerations are all zero. We start a pulse by imposing displacements on the bottom node over many time steps in both horizontal directions. Once the pulse has been generated, the displacement on the basal node remains at zero. We stop the calculation before the surface-reflected wave impinges on the artificial basal boundary and ascends back to the shallow region of interest. The method kinematically propagates waves through a linear elastic medium with the local velocity without dispersion. The nonlinear calculation is also nondispersive.

At the start of the time step at time t_0, the program knows displacement at the spatial grids $U_i\{t_0\}$ and the displacement field at the previous time step $U_i\{t_0 - \Delta t\}$, in which curly brackets indicate time steps and i is a horizontal direction. The difference between these quantities is the velocity a half-step before t_0, $V_i\{t_0 - \Delta t/2\} = (U_i\{t_0\} - U_i\{t_0 - \Delta t\})/\Delta t$. The code finds the new velocity at a half time step ahead from the acceleration at each grid point at time step t_0, $V_i\{t_0 + \Delta t/2\} = V_i\{t_0 - \Delta t/2\} + A_i\{t_0\}\Delta t$. The new displacement at $t_0 + \Delta t$ is $U_i\{t_0 + \Delta t\} = U_i\{t_0\} + V_i\{t_0 + \Delta t/2\}\Delta t$.

We illustrate spatial derivatives using an example group of adjacent displacement nodes (U, up; C, center; and D, down). The objective is to find the acceleration at time t_0. The shear traction between two nodes (down and center) is

$$\tau_{iz}(\mathrm{D,C})_{\{t_0\}} = G_\mathrm{U}\left[\frac{U_{i,\mathrm{D}} - U_{i,\mathrm{C}}}{\Delta Z}\right]_{\{t_0\}} - G_\mathrm{U}\varepsilon_i(\mathrm{D,C})_{\{t_0\}}, \quad \text{(A1)}$$

in which G_U is the shear modulus in the upper element, the first term represents elasticity, and $\varepsilon_i(\mathrm{D,C})$ is anelastic engineering strain. (This notation averts confusion with tensor indexes.) The acceleration of the center node from equation (5) is

$$A_{i,\mathrm{C}} = \frac{1}{\rho}\left[\frac{\tau_{iz}(\mathrm{D,C}) - \tau_{iz}(\mathrm{C,U})}{\Delta Z}\right]_{\{t_0\}}. \quad \text{(A2)}$$

The shear modulus G and anelastic strain ε_i in general depend on the current stress and history of the rock.

We represent anelastic strain with a coulomb-based flow law, qualitatively following Barbot and Fialko (2010). By assumption, many cracks are already present in the rock. The coefficient of friction of these cracks varies from low values to that of intact rock. Some cracks likely have prestress and fail at relatively low dynamic stresses of the right orientation (Marsan, 2005; Sleep, 2010). Macroscopic anelastic strain and, by assumption, the anelastic strain rate thus increase over a range of dynamic stresses, rather than at one plastic limit.

The numerical method seeks the smoothly varying predictable part of the particle velocity as would be recorded by surface seismograms and borehole arrays along with the distribution of anelastic strain at depth. It does not resolve the fate of individual cracks. That is, we exclude failure with sudden decreases of frictional strength and hence dynamic stress drop and brief pulses of seismic energy associated with crack failure. We do not attempt to resolve brief strong accelerations associated with this process.

Equation (A1) implies an anelastic strain rate at each node in which failure occurs. One requires that the rate of anelastic strain in equation (A1) be consistent with computed stress. Formally,

$$\tau_{iz}\{t_0\} = G_{\mathrm{U}}\left[\frac{U_{i,\mathrm{D}} - U_{i,\mathrm{C}}}{\Delta Z}\right]_{\{t_0\}} - G_{\mathrm{U}}\varepsilon_i\{t_0 - \Delta t\} - G_{\mathrm{U}}\left[\frac{\tau_{iz}\{t_0\}}{|\tau\{t_0\}|}\right]\Delta\varepsilon_i(|\tau\{t_0\}|), \tag{A3}$$

in which $\Delta\varepsilon_i(|\tau\{t_0\}|)$ is the anelastic strain during the time step; the expression is general and does not imply any specific rheology. The bracket in the third term causes the horizontal anelastic strain rate to be proportional to the components of the horizontal shear traction τ_{iz}. The shear traction (as τ_{iz} and $|\tau\{t_0\}|$) appears on both sides of equation (A3). The equation is readily solved by iteration if the anelastic strain rate increases smoothly and monotonically with stress. We let the anelastic strain (in the i direction and explicitly including the bracket in equation A3) per time step Δt function be

$$\Delta\varepsilon_i = \varepsilon^{'}\Delta t = \zeta\left[\frac{\tau_{iz}\{t_0\}}{|\tau\{t_0\}|}\right]\left[\frac{\tau_M}{G}\right]\left[\frac{|\tau\{t_0\}| - \tau_B}{\tau_M}\right]^m, \tag{A4}$$

in which anelastic strain has the sign to relieve stress, ζ is a dimensionless constant, $\tau_M = \rho g \mu_M z$ is a stress in which frictional creep becomes fast at the coulomb stress ratio μ_M, $\tau_B = \rho g \mu_B z$ implies that no anelastic strain occurs below a Bingham coefficient of friction of μ_B ($\varepsilon^{'} = 0; |\tau| \leq \tau_B$), and m is an exponent that represents rapid transition between slow and fast deformation as dynamic stress increases. Equation (A4) approaches a plastic yield surface in the limit of large m. The constant ζ then may be adjusted to obtain the desired transition stress between very slow and very fast creep. It is 1 in our calculations in the main article. We let $m = 5$ so that the models in the main article differ from simple plasticity; μ_M is 0.8 and μ_B is 0.3. For reference, the traditional coefficient of friction for crystalline rocks in the near surface is 0.85 (Byerlee, 1978). These parameters yield predicted peak ground velocity (PGV) similar to that observed at Lucerne in Figure 2.

Any smooth-calibrated monotonic function that increases slowly at low dynamic stresses and rapidly at large ones would have these basic properties. There are qualitatively only two free parameters in equation (A4) for generalization to a full 3D model: (1) the dynamic stress in which the effect of nonlinear attenuation exceeds that of ordinary attenuation and (2) the dynamic stress in which the anelastic strain rate becomes high enough that further increases in dynamic stress do not occur. We are not aware of any field data that would allow fine tuning equation (A4).

Department of Geophysics
Stanford University
Stanford, California 94305
norm@stanford.edu
(N.H.S.)

ConocoPhillips School of Geology and Geophysics
University of Oklahoma
Norman, Oklahoma 73019
(N.N.)

Manuscript received 28 October 2016;
Published Online 30 May 2017